International Journal of Nanomedicine

Dovepress
Taylor & Francis Group

Open Access Full Text Article

ORIGINAL RESEARCH

Theranostic Applications of Taurine-Derived Carbon Dots in Colorectal Cancer: Ferroptosis Induction and Multifaceted Antitumor Mechanisms

Rongrong Zhang[1,*], Shuting Lan[1,*], Mengxuan Jia[1,*], Fangyuan Liu[1], Mengqi Wang[2], Qin Jin[3], Liya Su[1], Gang Liu[1]

[1]Clinical Medicine Research Center, Affiliated Hospital of Inner Mongolia Medical University, Hohhot, Inner Mongolia, People's Republic of China; [2]College of Life Science and Oceanography, Weifang University, Weifang, Shandong, People's Republic of China; [3]Department of Pathology, Affiliated Hospital of Nantong University, Nantong, Jiangsu, People's Republic of China

*These authors contributed equally to this work

Correspondence: Gang Liu, Email 20190043@immu.edu.cn

Introduction: The theranostic potential of taurine-derived carbon dots (Tau/CDs) in colorectal cancer (CRC) remains largely unexplored, despite their promising physicochemical and biological properties.

Methods: In this study, Tau/CDs were synthesized via a microwave-assisted irradiation method, employing citric acid as the carbon source, urea as the nitrogen source, and taurine (Tau) as the dopant. Comprehensive physicochemical characterization and biocompatibility assessments were performed both in vitro and in vivo. The anti-cancer efficacy of Tau/CDs against CRC was systematically evaluated through a series of functional assays, including cell viability, proliferation, migration, invasion, adhesion, clonogenicity, cell cycle progression, apoptosis, epithelial-mesenchymal transition (EMT), and transcriptomic profiling. The therapeutic efficacy was further validated in vivo using CRC xenograft murine models.

Results: Tau/CDs exhibited excellent biocompatibility and significantly impaired key malignant properties of CRC cells, including viability, proliferation, migration, invasion, clonogenicity, and EMT. Treatment with Tau/CDs induced cell cycle arrest and apoptosis in vitro, while in vivo administration robustly suppressed tumor growth in xenograft models. Mechanistically, transcriptomic analysis combined with ferroptosis profiling identified Heme Oxygenase 1 (HO-1)-mediated ferroptosis as a critical pathway underlying the anti-tumor activity of Tau/CDs.

Conclusion: Microwave-assisted synthesis of Tau/CDs from citric acid, urea, and Tau yielded biocompatible nanoparticles with potent anti-cancer properties. Tau/CDs were shown to inhibit CRC progression by regulating multiple malignant phenotypes, with HO-1-mediated ferroptosis emerging as a critical mechanistic axis. These findings highlight Tau/CDs as a promising candidate for future clinical translation in CRC nanomedicine.

Keywords: taurine, carbon dots, colorectal cancer, ferroptosis, HO-1

Introduction

Despite declining incidence rates in high-income regions, colorectal cancer (CRC) remains one of the lethal malignancies globally, accounting for approximately 1.85 million new cases and 850,000 deaths annually.[1,2] Recurrence and metastasis represent the primary obstacles to achieving durable clinical remission. As the most prevalent malignancy of the digestive tract, CRC is largely driven by modifiable lifestyle factors, including physical inactivity, excessive consumption of sugars, salts, red and processed meats, alongside alcohol consumption, tobacco exposure, obesity, circadian rhythm disruption, and chronic psychological stress, all of which synergistically accelerate tumorigenesis and disease progression.[3] On the molecular level, CRC pathogenesis is governed by a complex interplay of genetic mutations and

Received: 22 January 2025
Accepted: 20 May 2025
Published: 16 June 2025

epigenetic alterations. These include chromosomal instability (CIN), microsatellite instability (MSI), CpG island methylator phenotype (CIMP), and mismatch repair gene deficiencies, which collectively orchestrate the multistep transformation of normal colonic epithelium into invasive and metastatic carcinoma.[4] Alarmingly, global projections suggest that CRC incidence will rise by 56% by 2040, reaching 3.2 million new cases and 1.6 million deaths annually.[1] This trend underscores the escalating public health and socioeconomic burden imposed by the disease.

Although current multimodal treatment regimens, comprising surgery, chemotherapy, radiotherapy, and molecularly targeted therapies, have significantly extended patient survival, the five-year survival rate for advanced-stage CRC remains dismally low, at less than 13%.[4–8] Moreover, the clinical benefits of existing therapies are constrained by limited drug bioavailability, dose-dependent toxicities, acquired drug resistance, and immune evasion escape. These persistent challenges highlight the urgent need for new therapeutic strategies capable of overcoming the biological and pharmacological barriers that limit current CRC treatments.[9]

In response to these challenges, nanotherapeutics have emerged as a transformative approach in oncological research.[10] Over the past few decades, substantial research efforts have been directed toward the development and clinical translation of nanoparticle-based platforms. Since the advent of cancer nanomedicine, the field has increasingly focused on engineering nanoparticles capable of precise pathological targeting while bypassing the inherent limitations of conventional therapeutic modalities.[11] Nanoparticles offer several attractive features, including facile synthesis, reduced systemic toxicity, robust chemical and mechanical stability, distinctive surface plasmon resonance, and effective photothermal conversion.[12] These properties have positioned nanotherapeutics at the forefront of cancer treatment innovation. However, despite their promise, several critical limitations persist. Nanotherapeutics often suffer from suboptimal surface charge, limited drug-loading capacity, proneness to aggregation, and poor tissue permeability, all of which restrict their therapeutic efficacy.[12] Moreover, their biocompatibility, structural stability, and degradation kinetics are highly sensitive to environmental variables such as irradiation, temperature shifts, and pH changes, often leading to premature drug leakage and uncontrolled release.[12] In addition, nanoparticles exhibit limited tumor accumulation, impaired deep-tumor penetration, and are rapidly cleared from circulation, further undermining their clinical potential.[11]

To address these limitations, a new generation of nanoformulations has been engineered and validated in both preclinical and clinical settings. Liposomes, gold-based metallic nanoparticles, and carbon quantum dots (CDs) have shown considerable promise in circumventing the therapeutic bottlenecks of conventional CRC treatments.[13] Their structural versatility and tunable biodegradability enable precise spatiotemporal control over drug release, enhance the therapeutic index, and mitigate drug resistance mechanisms, all while significantly reducing systemic toxicity.[13] Further studies suggest that the rational combination of engineered nanocarriers enhances the intratumoral drug accumulation and deep-tissue penetration while substantially lowering off-target toxicity.[13] Beyond conventional drug delivery, these functionalized nanoformulations reprogram the tumor immune microenvironment (TME) by stimulating antitumor immunity, reversing immunosuppression, and promoting the formation of long-lived memory immune cells, thereby amplifying the therapeutic efficacy of immunotherapy.[10] Together, these advances result in pronounced tumor suppression and improved long-term survival, underscoring the translational potential of nanoformulation-based therapeutics for CRC treatment.[10]

Among emerging nanocarriers, CDs stand out as a versatile class of carbon-based materials characterized by superior biocompatibility, tunable optical and electrical properties, high surface-to-volume ratios, and versatile structural architectures. These properties have enabled their broad application in bioimaging, cancer therapy, drug delivery, pollutant detection, optoelectronics, and biosensing.[14] Moreover, fabrication strategies, including precursor selection, post-synthesis modification, and surface functionalization, endow CDs with extraordinary flexibility, enabling their customization for specific biomedical applications.[14]

In light of recent research trends, amino acids have gained considerable attention as promising precursors for the synthesis of functional CDs, owing to their chemical diversity, biological relevance, and therapeutic potential.[15,16] Among them, taurine (Tau, 2-aminoethanesulfonic acid), a sulfur-containing, non-proteinogenic amino acid derived from cysteine and methionine, has attracted particular interest. Noted for its stability, water solubility, and widespread cellular distribution, Tau exhibits diverse biological activities, including antioxidant, anti-inflammatory, and anti-apoptotic properties.[17] Additionally, Tau modulates intracellular calcium homeostasis, supports post-translational

modification processes, maintains endoplasmic reticulum function, and stabilizes cellular membranes, highlighting its therapeutic relevance in a wide spectrum of diseases, such as cancer, cardiovascular disorders, neurodegenerative conditions, and metabolic syndromes.[17,18]

In the context of CDs synthesis, Tau has been employed as a functional dopant to endow CDs with improved biological performance. For instance, Sharma et al synthesized water-soluble Tau-derived CDs via thermal decomposition, confirming their bioimaging and anti-bacterial applications.[19] More recently, Hu et al prepared nitrogen- and sulfur-co-doped fluorescent CDs through a hydrothermal route using o-phenylenediamine and Tau as precursors, demonstrating their potential for mercury ion detection.[20] Despite these promising developments, the anti-cancer properties of Tau/CDs, particularly their potential mechanisms of action in CRC, remain insufficiently explored.

In this study, we report the synthesis of Tau/CDs via a microwave-assisted irradiation method, employing citric acid as a carbon source, urea as a nitrogen source, and Tau as a sulfur- and nitrogen-containing dopant. The structural and chemical properties of the resulting Tau/CDs were systematically characterized using transmission electron microscopy (TEM), X-ray photoelectron spectroscopy (XPS), and Fourier transform infrared spectroscopy (FTIR). Their biocompatibility was evaluated using both in vitro cell lines and in vivo murine models. Furthermore, the inhibitory effects of Tau/CDs on CRC progression were comprehensively validated, providing mechanistic insights and highlighting their potential as a novel therapeutic platform for CRC.

Materials and Methods

Chemicals

All chemicals used in this study were sourced from commercial suppliers, Thermo Fisher Scientific and Sigma-Aldrich, unless otherwise stated. All chemicals were used without further treatment.

Preparation and Characterization of Tau/CDs

Tau/CDs were synthesized by reacting 1.20 g Tau (T8691, Sigma-Aldrich), 3.0 g urea (U111897, Aladdin), and 3.0 g citric acid (C77920, Heowns) in 10.0 mL of distilled water. The mixture was subjected to microwave heating for 5 min, resulting in a black, foamy solid. The product was then ground in an agate mortar and cooled to room temperature. TEM images of the Tau/CDs were captured using a JEOL JEM-2100F field emission electron microscope. XPS analysis was performed with a Thermo Fisher Scientific XPS system employing Al Kα radiation (hv = 1486.6 eV). The binding energy for the C 1s line was referenced to 284.8 eV from adventitious carbon. FTIR spectra were recorded on an ALPHA FT-IR spectrometer, with wavelengths ranging from 370 to 7500 cm^{-1}, using the reflection method. UV-vis spectra of Tau/CDs in aqueous solution were obtained with an OCEAN OPTICS DH-2000-BAL spectrometer.

Ethics Statement and Animals

All animal-related experiments reported herein have been approved by the Institution Animal Care and Use Committee (IACUC) of Inner Mongolia Medical University (Approval ID SYXK [Meng] 2020–0003) and conducted in accordance with the National Institutes of Health guidelines for laboratory animal care. Mice were obtained from SPF (Beijing) Biotechnology Co., Ltd and housed in a pathogen-free facility with controlled environmental conditions (21±2 °C, 50 ±10% relative humidity, and a 12/12 h light/dark cycle). Throughout the experiment period, *ad libitum* access to sterilized food and water was provided.

To evaluate the in vivo biocompatibility of Tau/CDs, thirty male C57BL/6 mice (18–20 g, 6 weeks old) were used, meanwhile, ten female BALB/c nude mice (18–20 g, 5 weeks old) were used to evaluate the in vivo theranostic effect of Tau/CDs against CRC progression.

Cell Culture

Cell lines used to evaluate the in vitro biocompatibility of Tau/CDs included KGN (human ovarian granulosa cells), MACT (bovine mammary alveolar cells), HUCMSCs (human umbilical cord mesenchymal stem cells), and ARPE-19 (human retinal pigment epithelium cells). KGN (CL-0603, Procell) and ARPE-19 (CL-0026, Procell) cells were obtained

from Procell Life Science & Technology, while MACT cells were generously provided by Mr. Yuhao Chen (Inner Mongolia University). HUCMSCs were obtained from healthy donors with written informed consent in accordance with the Declaration of Helsinki and were kindly provided by Mrs. Shubin Li (Inner Mongolia People's Hospital).

All cell lines were cultured in their respective media (M-0603 for KGN cells, PM150210 for MACT cells, PM150312B for HUCMSCs, and CM-0026 for ARPE-19 cells, Procell) supplemented with 10% heat-inactivated fetal bovine serum (FBS, 164210, Procell), 100 U/mL penicillin/streptomycin antibiotics (P/S, PB180120, Procell), and 2 mm L-glutamine (PB180419, Procell) in a moistened and 5% CO_2 incubator.

For the theranostic applications of Tau/CDs against CRC progression, six CRC (Caco-2, HCT116, RKO, SW480, SW620, and LoVo) cell lines were applied. After cell thawing, these CRC cells were cultured under standard conditions (37 °C, 5% CO_2) in media specific to each line (CM-0050 for Caco-2 cells, PM150710 for HCT116 cells, PM150710 for RKO cells, CM-0223A for SW480 cells, CM-0225A for SW620 cells, and CM-0144 for LoVo cells, Procell). The Ethics Committee of Inner Mongolia Medical University approved the use of the abovementioned cell lines (Approval ID: 2024-5-513).

In vitro Biocompatibility Evaluation of Tau/CDs

According to the departmental protocols and these publications, with minor modifications, KGN, MACT, HUCMSCs, and ARPE-19 cells were exposed to 8 mg/mL of Tau/CDs for 72 h.[21,22] The cells, cultured in their respective media supplemented with an equivalent volume of their corresponding culture media, were set as the negative control (NC) group (n=3). Following a 72 h incubation period, the in vitro biocompatibility of Tau/CDs was assessed at 24, 48, and 72 h post-treatment using microscopic morphological evaluation and viability measurements performed with a Countess II Automated Cell Counter.[23]

An ex vivo hemolysis assay was performed to confirm the hemocompatibility of Tau/CDs.[24] Accordingly, the blood samples were collected from male C57BL/6 mice, centrifuged for 5 min, and dispersed in phosphate-buffered saline (PBS, P1020, Solarbio). The process was repeated thrice. Afterward, 200 μL supernatant was incubated with varying concentrations of Tau/CDs (1, 2, 4, and 8 mg/mL) at 37 °C for 1 h, and hemolysis was quantified by measuring absorbance at 570 nm (n=3).

In vivo Toxicity Evaluation

For in vivo toxicity evaluation, C57BL/6 mice were acclimatized for one week. A daily oral dose of 500 mg/kg body weight of Tau/CDs was administered to the Tau/CDs group,[17] while the NC group received normal saline daily (n=10). After 14 d, blood and feces samples were collected. Renal and hepatic functions were assessed by measuring serum levels of alanine aminotransferase (ALT), aspartate aminotransferase (AST), blood urea nitrogen (BUN), and creatinine (CRE) using a blood biochemical analyzer. Fecal samples were preserved for microbiome analysis using 16S rRNA gene sequencing with the aid of the Biomarker Biotechnology Co., Ltd.

Subsequently, all mice in both groups were weighed and euthanized, and tissue samples from the lungs, liver, spleen, and kidneys were completely excised, weighed, and totally immersed in the neutral buffered formalin solution (G2161, Solarbio) for the histological analysis. Organ coefficients, expressed as the ratio of organ wet weight to total body weight, were calculated for both groups.[25] After dehydration, paraffin embedding, preparation of 5-μm-thick paraffin sections, deparaffinization, and rehydration,[23] histological analysis including Hematoxylin and eosin (H&E) staining, Masson trichrome staining, and Periodic acid Schiff (PAS) staining of these sections were finally performed by commercial staining kits (GP1031 for H&E staining, GP1032 for Masson trichrome staining, and GP1039 for PAS staining, Servicebio) to validate the in vivo toxicity of Tau/CDs by analyzing pathological changes between both groups.

Cytotoxicity of Tau/CDs Against CRC Cells

The cytotoxicity of Tau/CDs against CRC cells was evaluated by the 3-(4,5-dimethylthiazol-2-yl-2,5-diphenyl tetrazolium bromide (MTT) assay.[26] All CRC cells were seeded in 96-well plates and cultured overnight. Then, these cells were treated with increasing concentrations of Tau/CDs (1, 2, 4, 8, and 16 mg/mL). These cells exposed to the same volume of Dulbecco's phosphate-buffered saline (DPBS, 14190250, Thermo Fisher Scientific) were accepted as the NC

group. At the indicated time points, MTT solution (C0009S, Beyotime) was added with the 96-well plates incubated for 2 h. After the addition of dimethyl sulfoxide (DMSO, 67–68-5, Coolaber) to solubilize the Formazan product, the absorbance at 570 nm was measured. The inhibitory rate (IR) of Tau/CDs on CRC cell proliferation was calculated (n=3).

EdU Staining Assay

To assess the proliferative capacities of CRC cells after Tau/CDs treatment, RKO cells of each treatment group (n=3) were incubated with the EdU click reaction buffer (C0071S, Beyotime) at 37 °C for 120 min, followed by DAPI (C0065, Solarbio) staining at 37 °C for 10 min.[23] The fluorescence intensity was microscopically recorded and quantified using Image J software.

Scratch Wound Healing Assay

A scratch wound healing assay was performed to confirm the migration abilities of CRC cells after Tau/CDs treatment.[23] Accordingly, RKO cells (5×10^3 cells/well) were seeded in 6-well plates in triplicate and cultured overnight. Prior to the Tau/CDs treatments, the cell monolayer with 95% confluence was scratched. After eliminating non-adhered cells and recording photomicrographs of the straight wounds at 0 h, RKO cells were exposed to Tau/CDs or DPBS (n=3). After 24 h, the migration into the scratched area was recorded with the wound closure rates calculated using ImageJ software by measuring the average areas of the final wound recorded at 24 h versus the initial one recorded at 0 h.

Transwell Invasion Assay

As previously described with slight modifications,[23] the invasiveness of CRC cells after Tau/CDs treatment was evaluated using a Transwell invasion assay. Briefly, RKO cells, resuspended by the serum-free medium containing Tau/CDs or DPBS (n=3), were seeded into the upper Transwell chambers, meanwhile, 600 μL of fresh medium was supplemented to the lower Transwell chambers. After cultivation for 24 h, the RKO cells remaining on the upper chamber side were removed. The lower chamber side was fixed in cold methanol at room temperature for 20 min and further stained with 0.1% crystal violet solution (C0121, Beyotime) for 15 min. The translocations through the membrane were microscopically recorded with the detailed cell counts analyzed using Image J software.

Clonogenicity Assessment

The malignant characteristic of CRC cells after Tau/CDs treatment was further confirmed by a clonogenicity assay.[23] For this purpose, RKO cells (n=3) were seeded in a 6-well plate, and cultured for an additional 8 d. The culture medium containing Tau/CDs or DPBS was changed every 72 h. Once the visible colonies developed, the colonies of each group were treated with 4% paraformaldehyde solution (PFA, P1110, Solarbio) for fixation. After the crystal violet staining, the colonies of both groups were microscopically examined and quantified using Image J software.

Adhesion Assessment

The malignancies of CRC cells after Tau/CDs treatment were analyzed by an adhesion assessment.[23] Accordingly, RKO cells post-Tau/CDs treatment (n=3) were seeded at the fibronectin-coated 96-well plates and culture for 30 min for cell attachment. After eliminating non-adhered cells, fixation by cold methanol, and crystal violet staining, adherent cells were microscopically photographed and enumerated using Image J software.

Cell Cycle Assay

To evaluate the effect of Tau/CDs treatments on cell cycle arrest in CRC cells, a cell cycle analysis kit (MA0334, Meilunbio) was used, as previously described.[23] Post-treatment, RKO cells (n=3) were detached, resuspended, and fixed in 70% ethanol at −20 °C overnight. Following the manufacturer's protocol, cells were stained with propidium iodide (PI)/RNA polymerase working solution at room temperature for 1 h in the dark. The cell suspension was then filtered through 70 μm nylon meshes (BD352350, Falcon) to remove clumps. Cell cycle distribution (G0/G1, S, and G2/M phases) was analyzed by flow cytometry (FACS) using a FACScan cytometer.

Apoptosis Assay

The apoptotic response to Tau/CDs treatments was assessed by Annexin V-FITC/PI staining.[23] After treatment, RKO cells (n=3) were collected, washed with cold DPBS, and incubated with Annexin V-FITC solution (CA1020, Solarbio) at 37 °C for 5 min in the dark. Following incubation, cells were stained with PI solution, and apoptosis was analyzed immediately using FACS.

In vivo Efficacy Assay

To effectively ascertain the therapeutic potency by a subcutaneous xenograft model, approximately 5×10^6 RKO cells in the logarithmic phase were collected and subcutaneously inoculated into the left underarm region of the BALB/c nude mice. When tumor volume reached a measurable size (designated as day 0), mice were treated with Tau/CDs (50 mg/kg body weight, peritumoral injections) or normal saline (NC group) every two days (n=5).[27] The subcutaneous tumor dimensions and body weight were monitored every two days using calipers and scales. On day 7 post-inoculation, all mice were anesthetized, and the blood samples were immediately collected via ocular puncture for the in vivo hepatorenal toxicity assessment. After euthanasia by CO_2 asphyxiation, xenograft tumors were surgically excised, weighed, and photographed. The maximum axis (L) and right-angle diameter to that axis (W) of tumors were measured with the terminal tumor volume calculated based on the equation (length × $width^2$)/2.[28]

Key organs (lung, liver, spleen, and kidney) were further excised, fixed, and embedded in paraffin blocks for H&E staining (n=3). Thereafter, terminal deoxynucleotidyl transferase-mediated dUTP nick end-labeling (TUNEL) staining, as well as immunofluorescence (IF) staining of xenograft tumors, were conducted to assess the therapeutic potency of Tau/CDs treatments in suppressing the in vivo CRC progression.

Paraffin-embedded xenograft tumor sections (n=3) were processed following standard protocols for dehydration, paraffin embedding, sectioning, deparaffinization, and rehydration.[29] Sections were incubated with Protease K solution (Servicebio, G1502) at 37 °C for 5 min, followed by equilibration at 37 °C for 30 min. Terminal deoxynucleotidyl transferase (TdT) enzyme labeling was performed at 37 °C for 1 h. After TdT enzyme buffer incubation at room temperature for 30 min, sections were counterstained with DAPI for 10 min in the dark. Finally, sections were mounted with an anti-fade mounting medium (S2100, Solarbio) and examined microscopically for TUNEL-positive cells (apoptotic cells). Apoptosis rates were quantified using ImageJ software.

For IF staining, paraffin-embedded tumor sections (n=3) were processed as described previously,[30] with minor modifications. After blocking non-specific binding with 10% bovine serum albumin (BSA, SW3015, Solarbio) at 37 °C for 30 min, sections were incubated at 4 °C overnight with primary antibodies targeting proliferation, apoptosis, metastasis, or angiogenesis markers, including KI-67, BAX, BCL-2, COX2, and VEGF. Sections were washed with PBS and incubated with appropriate secondary antibodies at 25 °C for 30 min. After counterstaining with DAPI, sections were microscopically analyzed, and fluorescence intensities were quantified using ImageJ software. A list of antibodies used is provided in Supplementation Table 1.

Transcriptomic Analysis

To investigate the molecular mechanisms underlying Tau/CDs treatments against CRC progression, total RNA was extracted from RKO cells (n=3) using Trizol reagent (Invitrogen). mRNA was enriched with Oligo (dT), fragmented, and reverse-transcribed into cDNA using the NEBNext Ultra RNA Library Prep Kit (7530, NEB). The cDNA was purified, end-repaired, and ligated with Illumina sequencing adapters, followed by PCR amplification. The cDNA library was sequenced on the Illumina HiSeq™ platform (Biomarker Biotechnology Co., Ltd). Raw sequencing data were processed by removing low-quality reads using Perl scripts. Clean reads were aligned to the human genome (hg19) with TopHat2. Gene expression levels were quantified using fragments per kilobase of exon per million fragments mapped (FPKM) and differentially expressed genes (DEGs) were identified using DESeq software. Only genes with a false discovery rate (FDR)<0.01 and an absolute log2 fold change≥2 were considered significant. DEGs were further analyzed using Gene Ontology (GO) and Kyoto Encyclopedia of Genes and Genomes (KEGG) enrichment through the Database for

Annotation, Visualization, and Integrated Discovery (DAVID) database. Gene Set Enrichment Analysis (GSEA) was used to examine the relationship between DEGs and signaling pathways.[25]

Ferroptosis Assessment

To confirm the results of the transcriptomic analysis and further elucidate the therapeutic potential of Tau/CDs in inducing ferroptosis and suppressing CRC progression, the effects of Tau/CDs treatments on ferroptosis in RKO cells were evaluated. Key indicators of ferroptosis were assessed, including intracellular ROS production, mitochondrial function, lipid peroxidation, levels of ferroptosis-related biochemical markers (GSH, MDA, and iron), and DNA damage.

Intracellular ROS levels were measured using a dichlorofluorescein diacetate (DCFH-DA) staining kit (S0033, Beyotime) as described previously.[23] Briefly, post-treatment RKO cells (n=3) were washed with DPBS and incubated with 10 μM DCFH-DA in serum-free medium at 37 °C for 30 min. Following DAPI counterstaining, ROS production was assessed microscopically and quantified using ImageJ software.

Mitochondrial dysfunction induced by Tau/CDs was analyzed using multiple assays.[31] MitoTracker staining (C1049, Beyotime) was employed to assess mitochondrial activity. Post-treatment RKO cells (n=3) were incubated with 200 nM MitoTracker reagent at 37 °C for 30 min, followed by DAPI counterstaining and imaging. MitoTracker intensity was quantified using ImageJ software. To determine mitochondrial membrane potential (ΔΨm), post-treatment RKO cells (n=3) were stained with 10 μM JC-1 working solution (C2006, Beyotime) for 20 min at 37 °C. The ΔΨm was assessed by imaging and analyzing JC-1 fluorescence intensity with ImageJ software. For ultrastructural analysis, mitochondrial damage was evaluated via TEM. Post-treatment RKO cells (n=3) were fixed with 2.5% glutaraldehyde (G1102, Solarbio) followed by post-fixation with 1% OsO_4, dehydration in ethanol, embedding, and sectioning. The prepared ultrathin sections were stained with uranyl acetate and lead citrate and then visualized using TEM.

Biochemical markers of ferroptosis (GSH, MDA, and iron content) in post-treatment cells (n=3) were assessed using commercial kits (S0052 for GSH, S0131 for MDA, Beyotime; BC5315 for iron, Solarbio).[23] Lipid peroxidation was evaluated using the C11-BODIPY 581/591 probe (C2006, Beyotime). Post-treatment cells (n=3) were incubated with 5 mm C11-BODIPY in a serum-free medium for 30 min, followed by DAPI counterstaining. Fluorescence intensity was analyzed microscopically and quantified using ImageJ software.

DNA damage was assessed by IF staining of γH2A.X and the comet assay.[23] For IF staining, post-treatment RKO cells (n=3) were fixed in PFA, permeabilized with 0.5% Triton X-100 (T8200, Solarbio), and blocked with BSA. The cells were then incubated with a rabbit anti-γH2A.X antibody at 4 °C overnight, followed by secondary antibody incubation for 1 h. After DAPI counterstaining, γH2A.X staining intensity was measured microscopically using ImageJ software. The list of antibodies used is provided in Supplementation Table 1.

For the comet assay, post-treatment RKO cells (n=3) were mixed with 0.7% low-melting agarose and applied to slides pre-coated with 1.0% normal-melting agarose (C2041M, Beyotime).[32] Following lysis with ice-cold buffer for 4 h, the slides were subjected to alkaline electrophoresis for 30 min at 25 V, neutralized, stained with PI, and examined microscopically. DNA damage was quantified based on comet tail length and intensity.

Protein Preparation and Western Blot

To evaluate the expression of proteins involved in EMT, apoptosis, and ferroptosis, Western blot was performed.[33] Total protein was extracted from post-treatment RKO cells (n=3) using a protein extraction kit (DE101, Transgen) and quantified with a BCA assay kit (PC0020, Solarbio). Equal amounts of protein (30 μg) were resolved by Sodium Dodecyl Sulfate-Polyacrylamide Gel Electrophoresis (SDS-PAGE, P1200, Solarbio) and transferred to PVDF membranes (PVH00010, Millipore). After blocking with 5% skim milk (A600669, Sangon) for 30 min, membranes were incubated with primary antibodies at 4 °C overnight. After washing with 0.1% Tween-20 in Tris-HCl, membranes were incubated with HRP-conjugated secondary antibodies at room temperature for 1 h. Protein bands were visualized using an enhanced chemiluminescence (ECL) solution (MA0186, Meilunbio) and imaged using ChampChemi. Band intensities were quantified using ImageJ software and normalized to GAPDH expression. The antibodies used are listed in Supplementation Table 1.

Statistical Analysis

Each experiment was performed in triplicate unless otherwise stated. The analyses and plotting of experimental data in this study were performed using GraphPad Prism software (v9.0), Statistical Package for the Social Sciences software (SPSS, v19.0), and R software (v4.0.0). The descriptive data were analyzed by the Student's *t*-test and were presented as mean ± standard deviations (SD) unless otherwise noted. A probability value of $P<0.001$ was considered to be extremely significant, $P<0.01$ indicated very significant, $P<0.05$ indicated statistically significant, and $P>0.05$ indicated not significant (ns).

Result

Physicochemical Characterization of Tau/CDs

The synthesized Tau/CDs predominantly exhibited a uniform, spherical morphology with minor aggregation, as observed via TEM (Figure 1A). XRD analysis revealed a broad diffraction peak centered at $2\theta = 25.5°$, corresponding to the (002) plane of graphitic carbon, indicative of a partially crystalline carbon framework (Figure 1B). FTIR confirmed the presence of characteristic functional groups, including O-H and N-H stretching vibrations at 3427 cm^{-1} and 3202 cm^{-1}, respectively. Notably, ester and carbonyl (C=O) bands appeared at 1710 cm^{-1} and 1617 cm^{-1} (Figure 1C). Peaks at 1443–1414 cm^{-1} were attributed to C-N stretching, and those between 630–650 cm^{-1} to terminal ≡ C-H bending. XPS analysis further validated the elemental composition of the Tau/CDs, revealing 51.55% carbon, 26.33% oxygen, 17.95% nitrogen, and 4.17% sulfur (Figure 1D). Deconvolution of the high-resolution N 1s spectrum indicated pyrrole- and pyridine-type nitrogen species, implying the formation of a conjugated aromatic core structure. Fluorescence spectroscopy demonstrated that the Tau/CDs exhibited a strong emission peak at 374 nm upon 365 nm excitation (Supplementation Figure 1), a phenomenon attributed to aromatic C=C and C=N conjugation coupled with surface amino and sodium functional groups. Consistent with these observations, UV-Vis spectroscopy (200–400 nm)

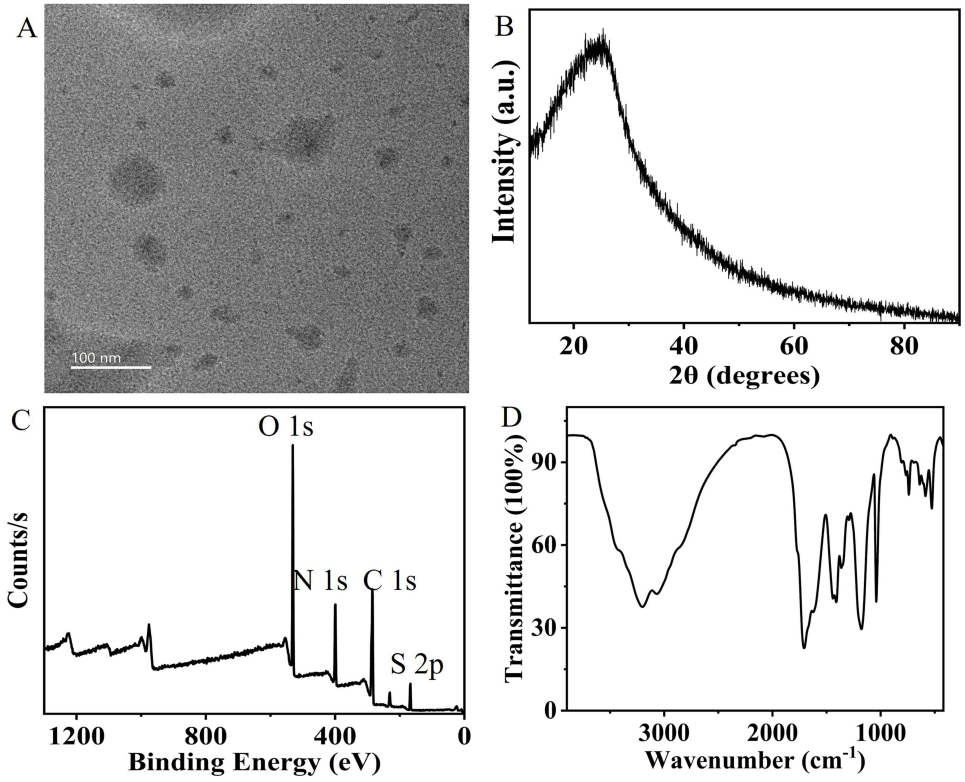

Figure 1 Physicochemical characterization of Tau/CDs. (**A**) TEM image displaying the morphology of Tau/CDs. (**B**) XRD pattern of Tau/CDs recorded from 5° to 90°. (**C**) XPS survey spectrum confirming the elemental composition of Tau/CDs. (**D**) FTIR spectrum illustrating surface functional groups of Tau/CDs.

supported the existence of π-π* transitions associated with pyrrole- and pyridine-type nitrogen dopants, reinforcing the structural interpretation of a conjugated core-state (CS) architecture.

Biocompatibility Evaluation of Tau/CDs

The cytocompatibility of Tau/CDs was assessed across multiple cell lines, including KGN, MACT, HUCMSCs, and ARPE-19. No statistically significant reductions in cell viability were observed after 24, 48, or 72 h of incubation when compared to the NC group (Figure 2), underscoring their excellent biocompatibility. Hemolysis assays further confirmed that the hemolytic activity of Tau/CDs remained consistently below the 10% threshold, meeting the accepted safety criteria (Supplementation Figure 2).

Subsequent in vivo biosafety evaluation in murine models corroborated these findings. Mice exposed to Tau/CDs exhibited normal weight gain, physiological behavior, and survival rates throughout the experimental timeline (Supplementation Figure 3). Organ-to-body weight indices (liver, lungs, kidneys, spleen) and serum biomarkers, including ALT, AST, BUN, and CRE, showed no statistically significant deviations from the NC group (Supplementation Figure 3). Histopathological analysis of major organs using H&E, Masson trichrome, and PAS staining confirmed the absence of observable morphological abnormalities (Figure 3).

Moreover, 16S rRNA gene sequencing of fecal samples revealed no significant alterations in gut microbiome diversity following Tau/CDs treatment. The α diversity indices, as Chao1 (Figure 4A), Simpson (Figure 4B), Shannon (Figure 4C), and ACE (Figure 4D), were statistically indistinguishable between the Tau/CDs-treated and NC groups. Principal component analysis (PCA) of β diversity at both genus (Figure 4E) and species (Figure 4F) levels demonstrated no significant microbial community shifts ($P>0.05$). As shown in Figure 4G, the community histogram analysis at the genus level revealed that the Tau/CDs treatment decreased the relative abundance of *uncultured remen bacterium, Unclassified_Clostridia_UCG-014, Candidatus Arthromitus*, and *Dubosiella*, as well as promoted the relative abundance of *Ligilactobacillus, Lactobacillus, Bacteroides, uncultured_Bacteroidales_bacterium*, and *Lachnospiraceae_NK4A136_ group*. Moreover, the community histogram analysis at the species level, shown in Figure 4H, revealed that the Tau/CDs treatment decreased the relative abundance of *Limosilactobacillus_reuteri, Clostridioides_difficile, unclassified_Clostridia_UCG_014, Firmicutes_bacterium_M10_2*, and *uncultured_rumen_bacterium*, as well as promoted the relative abundance of *Lactobacillus_johnsonii, Ligilactobacillus _murinus, uncultured_ Bacteroidales_bacterium*, and *unclassified_Lachnospiraceae_NK4A136_ group*. Therefore, these comprehensive results effectively clarify the excellent biocompatibility of Tau/CDs both in vitro and in vivo.

In vitro Therapeutic Effects of Tau/CDs Against CRC

As depicted in Supplementation Figure 4, the MTT assay demonstrated the robust inhibitory effects of Tau/CDs on the proliferation of CRC cells, characterized by a dose-dependent reduction in viability across all Tau/CDs treatment groups relative to the NC group. Given the significant intergroup differences in viability, an optimal concentration of 4 mg/mL Tau/CDs and RKO cells was selected for further analyses.

As anticipated, the EdU incorporation assay results paralleled the MTT data, revealing a substantial decline in the ratio of EdU-positive cells to total DAPI-positive cells in the Tau/CDs-treated group (Figure 5A and B, $P<0.05$). Beyond inhibiting proliferation, Tau/CDs significantly impaired oncogenic behaviors, including migration (Figure 5C and D, $P<0.05$), invasion (Figure 5E and F, $P<0.05$), clonogenicity (Figure 5G and H, $P<0.05$), and adhesion (Figure 5I and J, $P<0.05$). Additionally, Tau/CDs treatment induced pronounced cell cycle perturbation (Figure 5K and L, $P<0.05$) and promoted apoptosis in RKO cells (Figure 5M and N, $P<0.05$).

Consistently, the molecular basis of these therapeutic effects of Tau/CDs was underscored by the differential expression patterns of EMT-related proteins (E-CADHERIN, VIMENTIN, N-CADHERIN, and SLUG) and apoptosis regulators (BAX, BCL-2, and CASPASE 3) between the Tau/CDs and NC groups (Figure 5O & Supplementation Figure 5, $P<0.05$).

Collectively, these aforementioned findings underscored the potent therapeutic efficacy of Tau/CDs in disrupting key survival, proliferative, migratory, invasive, clonogenic, adhesive, and EMT-associated processes in RKO cells while promoting significant cell cycle perturbation and apoptosis, positioning Tau/CDs as promising candidates for future therapeutic intervention in CRC.

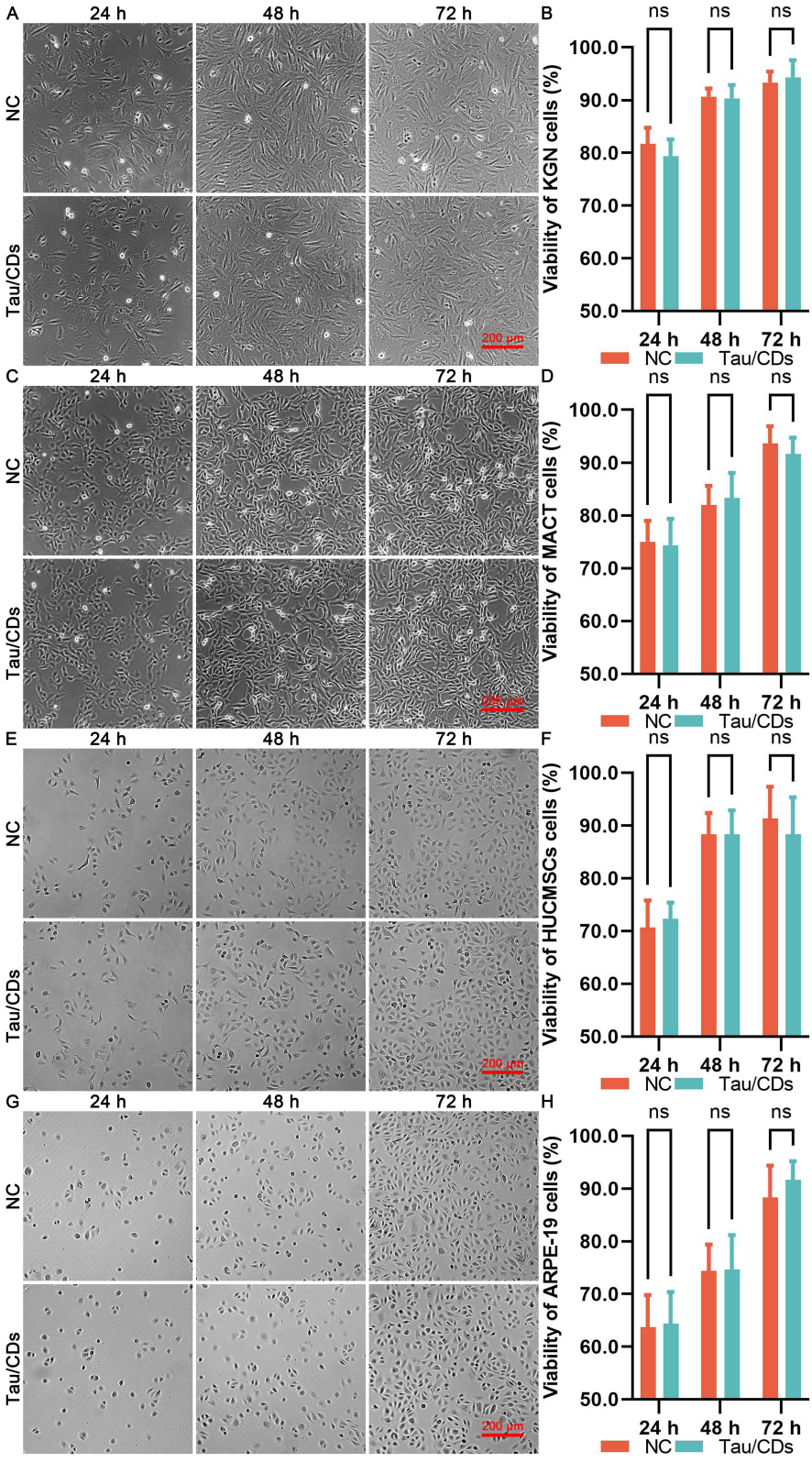

Figure 2 In vitro biocompatibility evaluation of Tau/CDs in multiple cell lines. (**A**) Morphological assessment of KGN cells after 24, 48, and 72 h of Tau/CDs exposure. (**B**) Cell viability of KGN cells treated with Tau/CDs for 24, 48, and 72 h. (**C**) Morphological assessment of MACT cells following Tau/CDs treatment for 24, 48, and 72 h. (**D**) Cell viability of MACT cells after Tau/CDs treatment for 24, 48, and 72 h. (**E**) Morphological assessment of HUCMSCs after Tau/CDs treatment at 24, 48, and 72 h. (**F**) Cell viability of HUCMSCs following Tau/CDs exposure for 24, 48, and 72 h. (**G**) Morphological assessment of ARPE-19 cells after 24, 48, and 72 h of Tau/CDs treatment. (**H**) Cell viability of ARPE-19 cells after exposure to Tau/CDs for 24, 48, and 72 h. Statistical significance: ns indicates no significant difference (P>0.05).

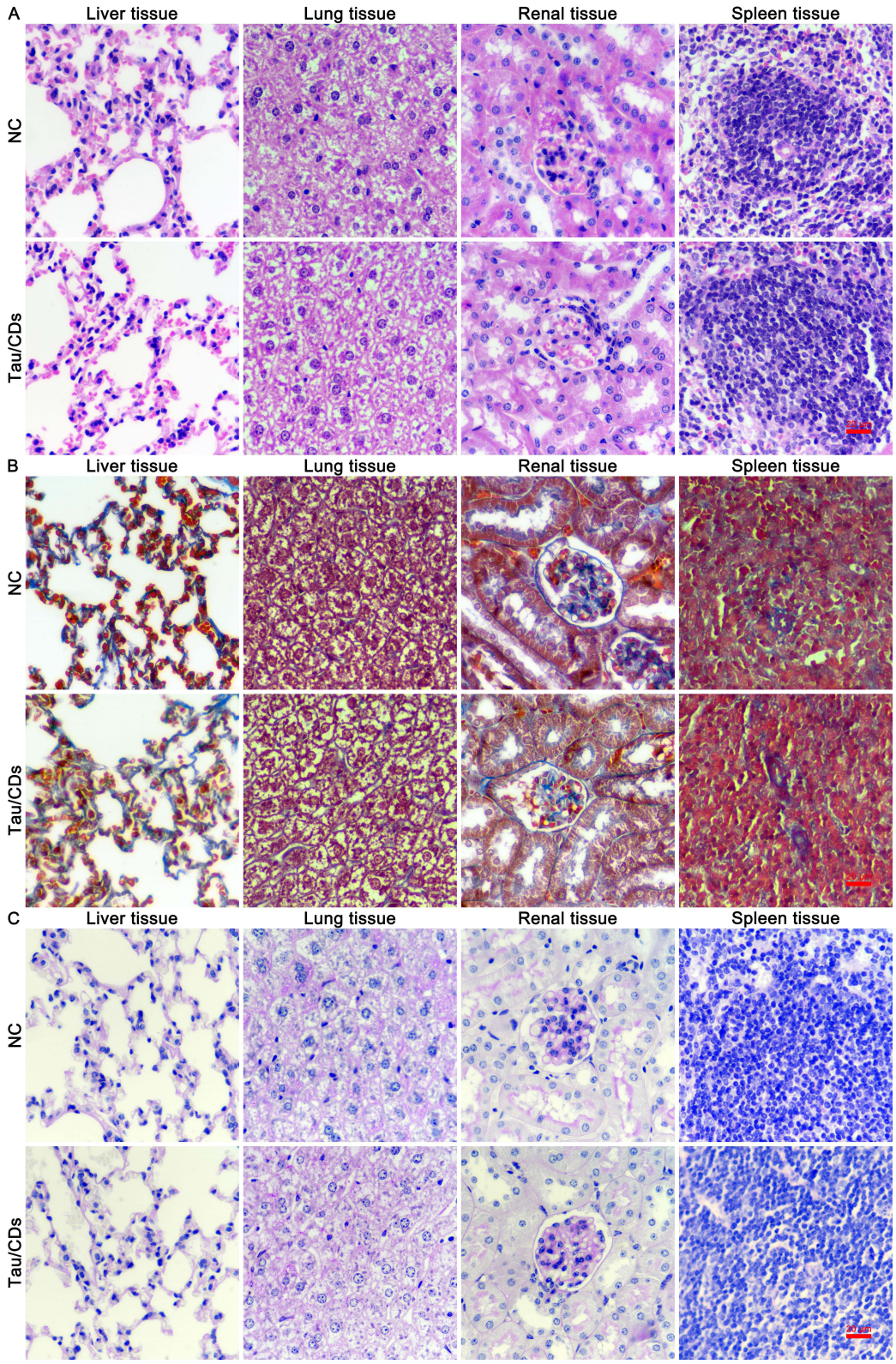

Figure 3 In vivo biocompatibility of Tau/CDs in C57BL/6 mice. (**A**) H&E staining of major organs collected from Tau/CDs-treated C57BL/6 mice. (**B**) Masson trichrome staining of major organs from Tau/CDs-treated C57BL/6 mice. (**C**) PAS staining of major organs from Tau/CDs-treated C57BL/6 mice. No histopathological abnormalities were observed.

https://doi.org/10.2147/IJN.S516926

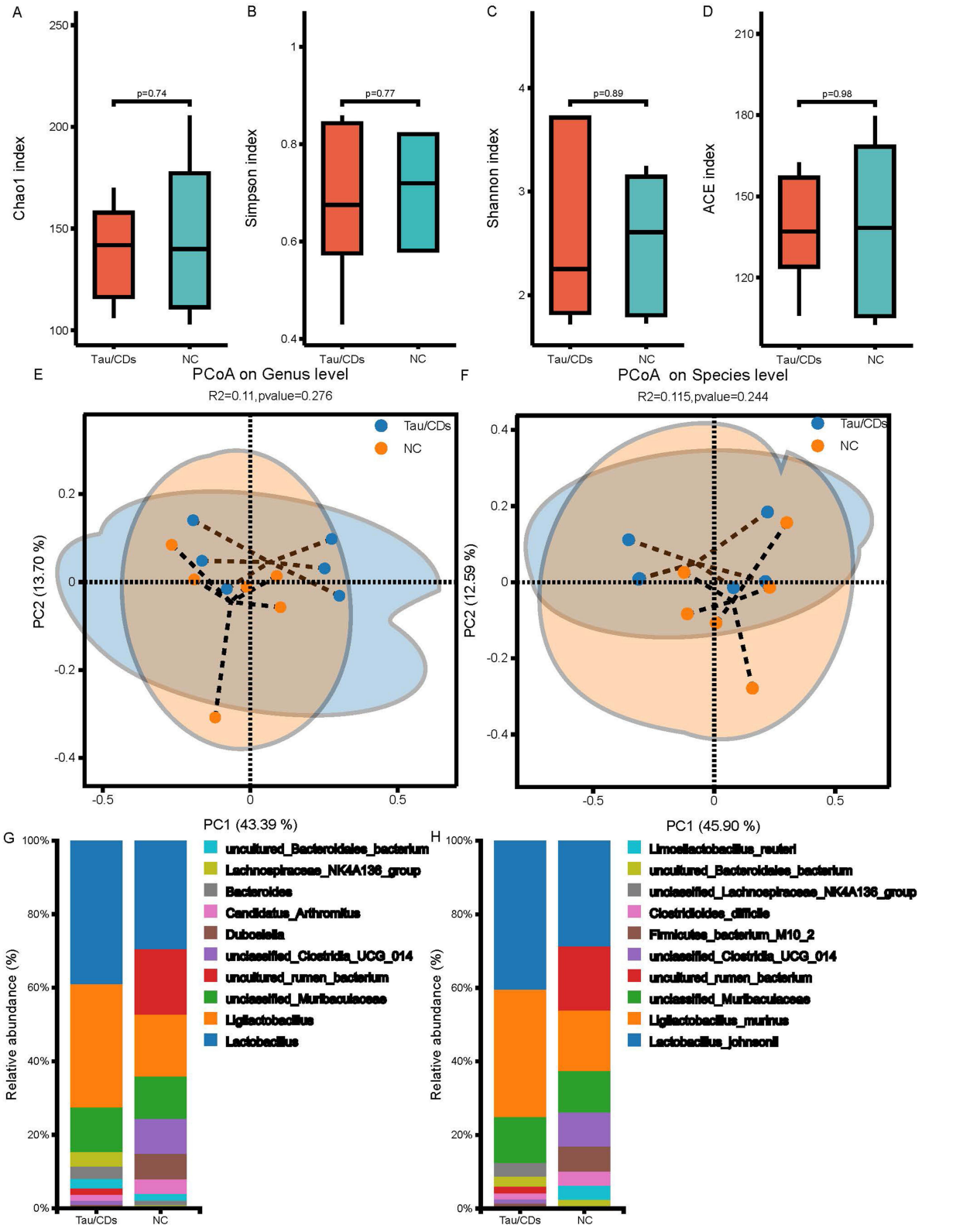

Figure 4 Influence of Tau/CDs on gut microbiota composition and diversity in C57BL/6 mice. (**A**) Chao index analysis to evaluate species richness. (**B**) Simpson index analysis to assess species evenness. (**C**) Shannon index analysis indicating species diversity. (**D**) ACE index analysis reflecting species abundance. (**E**) PCoA of β diversity at the genus level. (**F**) PCoA of β diversity at the species level. (**G**) Relative abundance of gut microbiota at the genus level. (**H**) Relative abundance of gut microbiota at the species level.

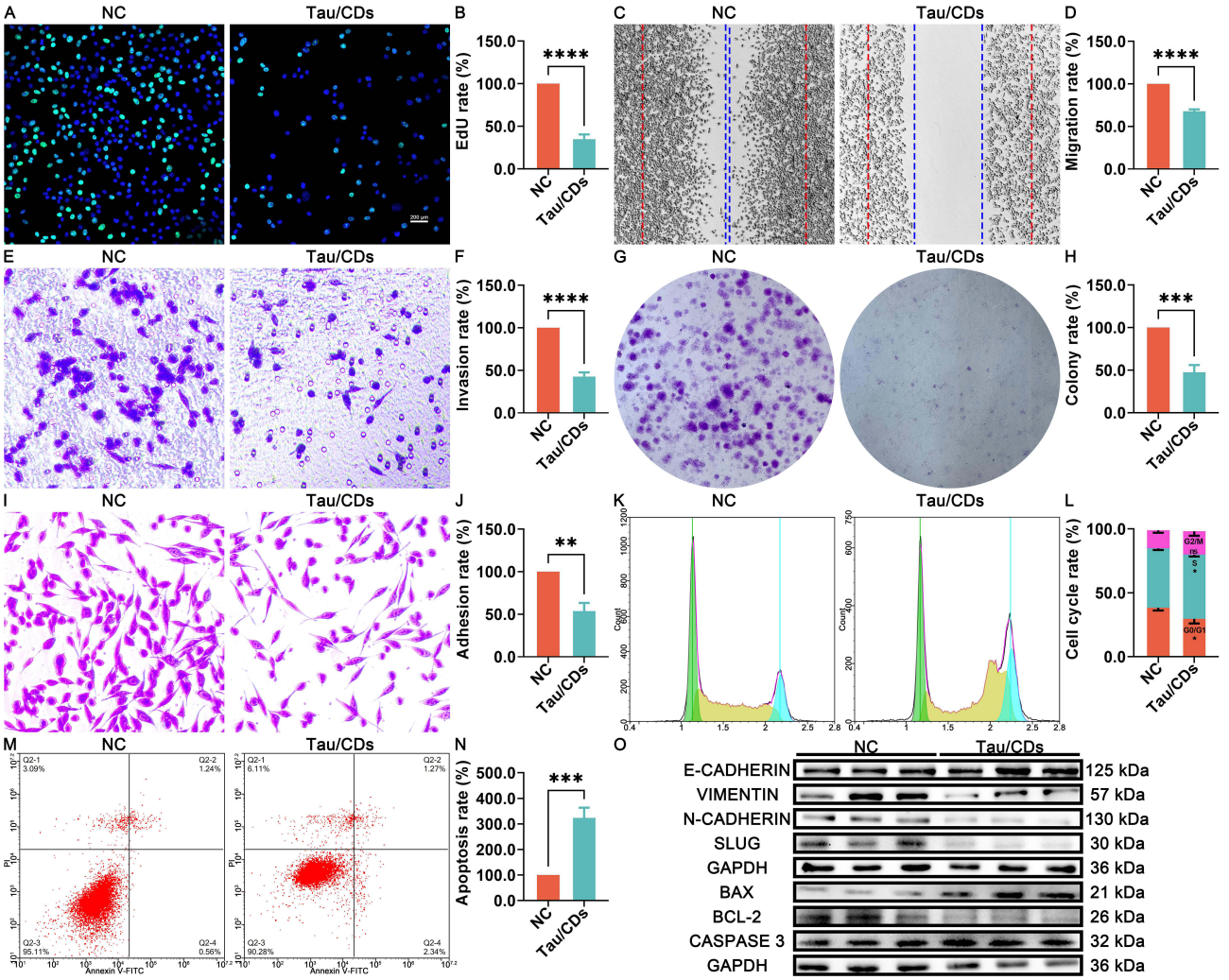

Figure 5 Tau/CDs suppress the malignant behaviors of RKO cells. (**A**) EdU staining for proliferation assessment of RKO cells treated with Tau/CDs. (**B**) Quantification of EdU-positive cells. (**C**) Representative images of the RKO cell migration assay after Tau/CDs treatment. (**D**) Quantitative analysis of migrated cells. (**E**) Representative images of RKO cell invasion assay. (**F**) Quantitative analysis of invaded cells. (**G**) Clonogenic assay showing colony formation ability of RKO cells post-treatment. (**H**) Quantification of colony numbers. (**I**) Cell adhesion assay of RKO cells after Tau/CDs exposure. (**J**) Quantitative analysis of adhered cells. (**K**) Flow cytometric analysis of the cell cycle distribution in RKO cells. (**L**) Statistical summary of the percentage of cells in each cell cycle phase. (**M**) FACS plots of Annexin V/PI staining for apoptosis detection. (**N**) Quantification of apoptosis rate in RKO cells. (**O**) Western blot analysis of EMT markers and apoptosis-related proteins. ns indicates no significant difference (P>0.05) with * representing P<0.05, ** representing P<0.01, *** representing P<0.001, and **** representing P<0.0001.

In vivo Therapeutic Efficacy of Tau/CDs in CRC Xenografts

Building upon the promising in vitro therapeutic potential of Tau/CDs, the in vivo anti-tumor efficacy of Tau/CDs was next assessed using an RKO xenograft murine model. Throughout the whole treatment period, the body weights of the mice remained stable across all groups, with no significant fluctuations observed (Supplementation Figure 6, P>0.05), suggesting the in vivo tolerability of Tau/CDs. In contrast, treatment with Tau/CDs significantly suppressed the tumor growth compared to the NC group (Figure 6A, P<0.05). Post-sacrifice analyses demonstrated substantial reductions in the tumor weight (Figure 6B and C, P<0.05) in the Tau/CDs-treated cohort.

Histopathological analyses supported these findings. H&E staining revealed extensive tumor cell shrinkage and nuclear fragmentation in the Tau/CDs-treated tissues (Figure 6D). TUNEL assays corroborated these results by demonstrating elevated apoptotic cell fractions in the Tau/CDs-treated tumors compared with the NC group (Figure 6E and F, P<0.05). The IF staining further confirmed the downregulation of proliferation (KI-67, Figure 6G and H, P<0.05), anti-apoptosis (BCL-2, Figure 6K and L, P<0.05), pro-metastatic (COX-2, Figure 6M and N, P<0.05), and angiogenesis (VEGF, Figure 6O and P, P<0.05) markers, along with increased expression of the pro-apoptotic protein BAX (Figure 6I and J, P<0.05) in the Tau/

https://doi.org/10.2147/IJN.S516926

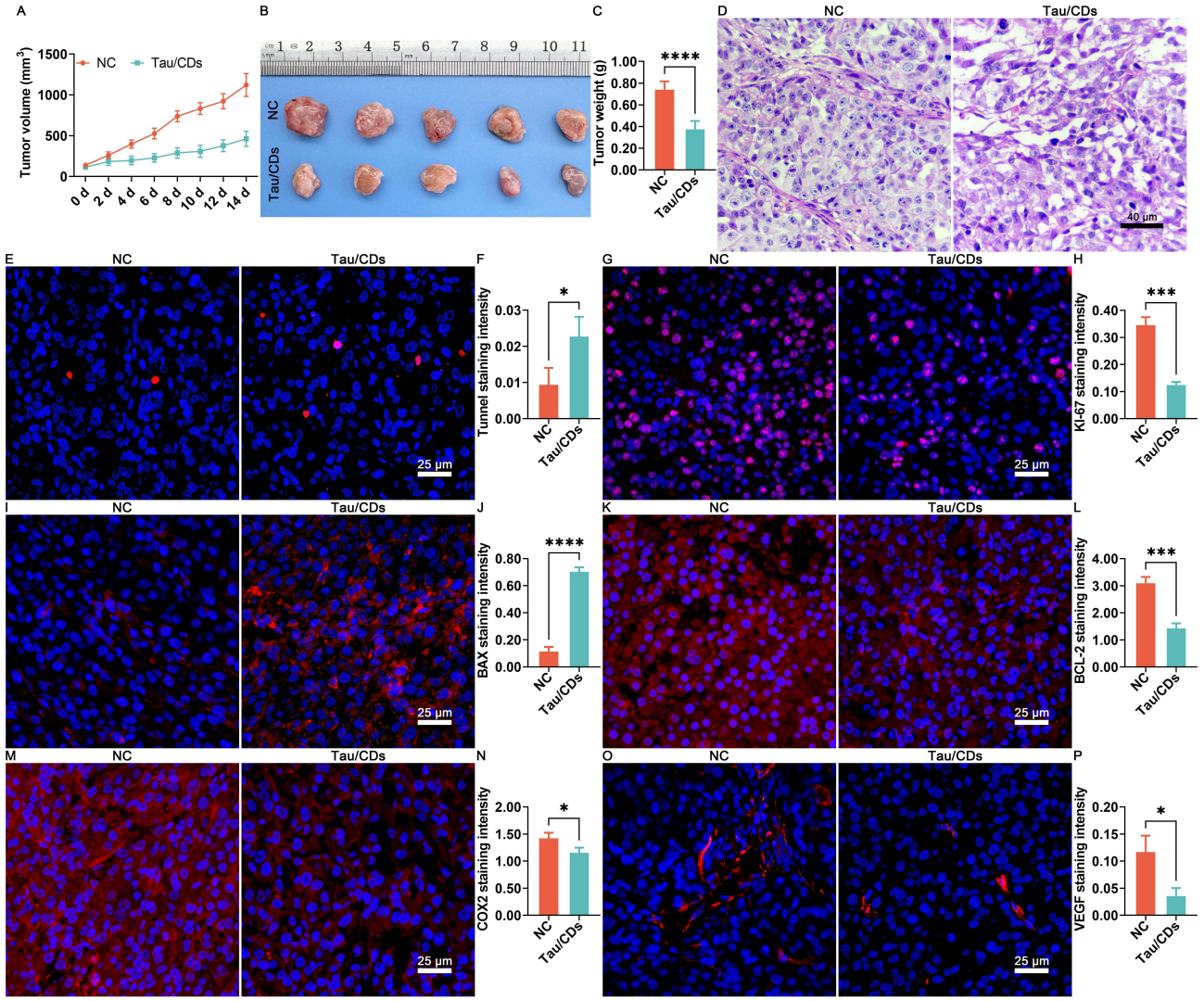

Figure 6 In vivo antitumor efficacy of Tau/CDs against CRC progression in xenograft models. (**A**) Growth curve of xenograft tumors following Tau/CDs administration. (**B**) Representative macroscopic images of xenograft tumors. (**C**) Quantification of tumor weights. (**D**) H&E staining of xenograft tumor sections. (**E**) TUNEL staining illustrating apoptotic cells within tumors. (**F**) Quantification of TUNE-positive cells. (**G**) IF staining of KI-67 in tumor sections. (**H**) Quantification of KI-67-positive cells. (**I**) IF staining of BAX protein expression. (**J**) Quantification of BAX-positive cells. (**K**) IF staining of BCL-2 protein expression. (**L**) Quantification of BCL-2-positive cells. (**M**) IF staining of COX-2 protein expression. (**N**) Quantification of COX-2-positive cells. (**O**) IF staining of VEGF protein expression. (**P**) Quantification of VEGF-positive cells. * represents P<0.05, with *** representing P<0.001 and **** representing P<0.0001.

CDs group. Collectively, these findings underscored the potent therapeutic activity of Tau/CDs against in vivo CRC progression through suppressing proliferation, metastasis, and angiogenesis while promoting apoptosis.

Complementary analyses of organ histology and serum biochemistry were also performed to reaffirm the in vivo safety profile of Tau/CDs. No significant differences were observed in the organ index (Supplementation Figure 6, P<0.05), in line with stable levels of liver and renal function indexes, with respect to ALT (P<0.05), AST (P<0.05), BUN (P<0.05), and CRE (P<0.05) between the Tau/CDs and NC groups (Supplementation Figure 6). Correlating with the ex vivo biocompatibility results, the absence of histopathological abnormalities in the main organs (Supplementation Figure 6) further highlighted the favorable biocompatibility of Tau/CDs and reinforced their potential as a safe and efficacious therapeutic strategy.

Molecular Features Underlying the Therapeutic Effects of Tau/CDs in CRC Progression

To elucidate the intrinsic molecular mechanisms driving the therapeutic efficacy of Tau/CDs against CRC progression, transcriptomic profiling was performed on RKO cells following Tau/CDs exposure. A total of 12,595 transcripts were detected, with 1155 genes significantly dysregulated in response to Tau/CDs treatment, comprising 548 upregulated and

607 downregulated genes (Figure 7A). Hierarchical clustering visualized distinct gene expression patterns between both groups (Figure 7B), highlighting the profound transcriptional reprogramming induced by Tau/CDs.

GO enrichment analysis of DEGs revealed significant enrichment in biological processes, including response to oxidative stress, regulation of epithelial cell proliferation, regulation of apoptotic signaling pathway, regulation of actin filament-based process, telomere organization, cellular response to oxidative stress, extrinsic apoptotic signaling pathway,

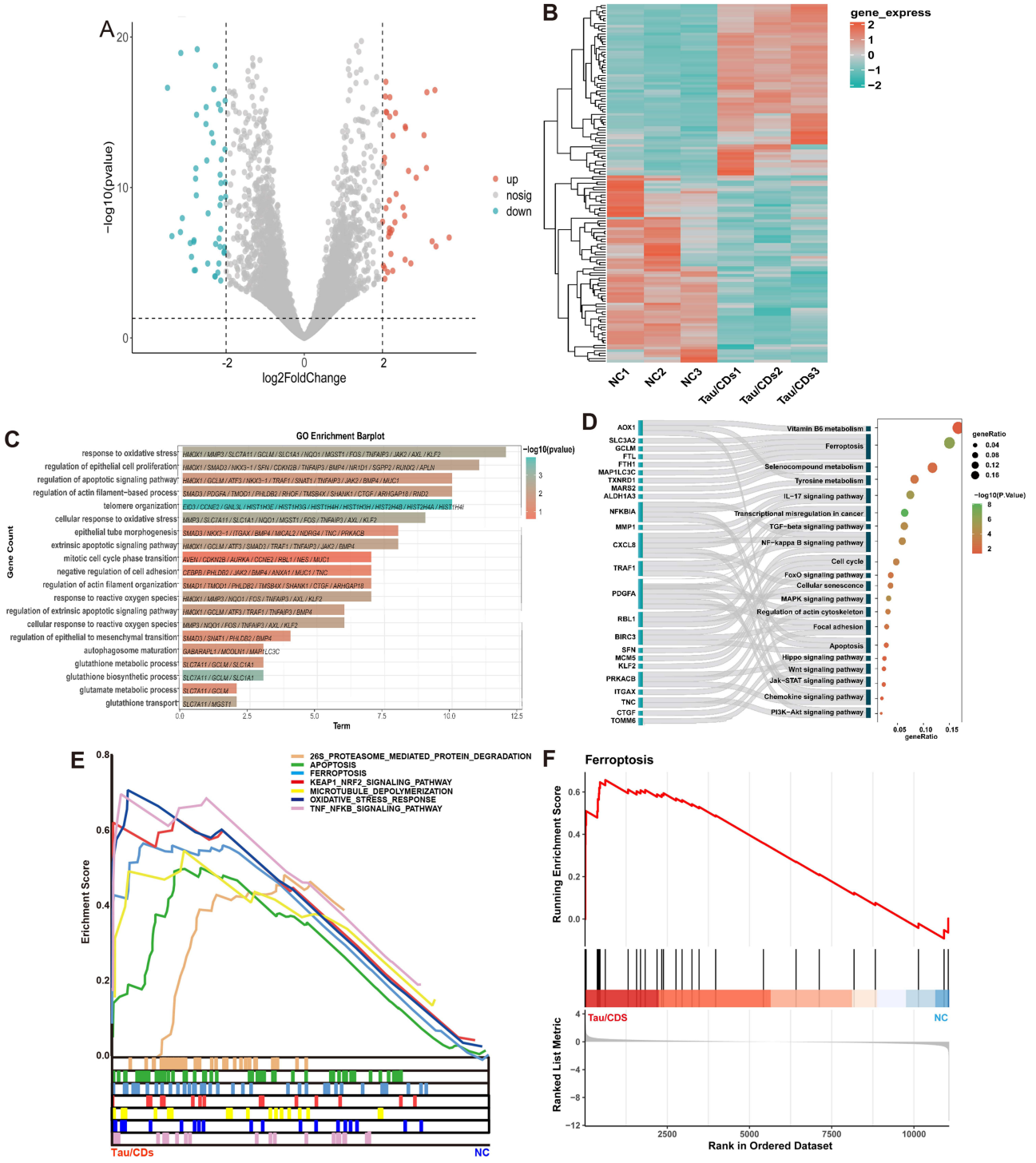

Figure 7 Transcriptomic alterations induced by Tau/CDs in RKO cells. (**A**) Volcano plot showing DEGs following Tau/CDs treatment. (**B**) Heat map illustrating expression patterns of DEGs. (**C**) GO biological process enrichment analysis of DEGs. (**D**) KEGG pathway enrichment analysis of DEGs. (**E**) GSEA enrichment plot showing significant KEGG signaling pathways. (**F**) GSEA highlighting ferroptosis-related pathway enrichment.

https://doi.org/10.2147/IJN.S516926

mitotic cell cycle phase transition, negative regulation of cell adhesion, and regulation of actin filament organization (Figure 7C). These functional categories aligned closely with the observed cellular phenotypes, particularly the Tau/CDs-induced impairments in proliferation, invasion, and survival.

Further pathway enrichment analysis using KEGG indicated that Tau/CDs treatment modulated multiple oncogenic and stress-response pathways, including vitamin B6 metabolism, ferroptosis, selenocompound metabolism, tyrosine metabolism, IL-17 signaling, transcriptional misregulation in cancer, TGF-β signaling, NF-κB signaling, and cell cycle regulation (Figure 7D). GSEA further highlighted seven positively enriched pathways in the Tau/CDs-treated group, including the 26S proteasome-mediated protein degradation, apoptosis, ferroptosis, KEAP1-NFR2 signaling pathway, microtubule depolymerization, oxidative stress response, and the TNF NF-κB signaling pathway (Figure 7E). Strikingly, ferroptosis, a regulated, iron-dependent form of non-apoptotic cell death, emerged as a recurrent and central pathway in both KEGG and GSEA analyses (Figure 7F). These findings suggested that ferroptosis induction might play a pivotal role in the therapeutic action of Tau/CDs.

Tau/CDs Induce Ferroptosis in CRC Cells

To experimentally validate the transcriptomic prediction, hallmark indices of ferroptosis were systematically assessed in Tau/CDs-treated RKO cells.

ROS production, a canonical trigger of ferroptosis, was significantly elevated in the Tau/CDs-treated RKO cells, as evidenced by increased DCFH-DA fluorescence intensity from the NC group to the Tau/CDs group (Figures 8A and B, $P<0.05$). This redox imbalance was accompanied by pronounced mitochondrial dysfunction in the Tau/CDs-treated RKO cells, as indicated by decreased MitoTracker fluorescence (Figure 8C and D, $P<0.05$), disrupted $\Delta\Psi m$ (Figure 8E and F, $P<0.05$), and increased mitochondrial damages (Figure 8G and H, $P<0.05$) compared with the NC group.

In parallel, markers of lipid peroxidation, another key ferroptotic signature, were elevated. MDA levels (Figure 8J, $P<0.05$) and lipid peroxide accumulation (Figure 8L and M, $P<0. 05$) were significantly increased in Tau/CDs-treated cells, signifying heightened lipid peroxidation. Reduced intracellular GSH levels (Figure 8I, $P<0.05$) and elevated intracellular iron content (Figure 8K, $P<0.05$) provided further evidence of ferroptotic cell death induced by Tau/CDs treatments.

Western blot confirmed that Tau/CDs modulated the expression of ferroptosis-regulatory proteins, including KEAP1, NRF2, HO-1, SLC7A11, and GPX4 (Figure 8R & Supplementation Figure 7, $P<0.05$). Moreover, IF imaging of xenograft tumors validated the upregulation of HO-1, VDAC1, and NRF2 in Tau/CDs-treated samples (Supplementation Figure 8, $P<0.05$), reinforcing the therapeutic potential of Tau/CDs in CRC by initiating ferroptosis.

Given the emerging link between ferroptosis and DNA damage,[34] additional DNA damage assays were performed. Enhanced γH2A.X staining intensity (Figure 8N and O, $P<0.05$), elevated comet tail DNA fragmentation (Figure 8P and Q, $P<0.05$), and upregulation of DNA damage response kinases ATM and ATR (Figure 8R & Supplementation Figure 7, $P<0.05$) all pointed to a secondary DNA damage response during Tau/CDs-induced ferroptosis.

In addition, ferrostatin-1 (Fer-1, a specific ferroptosis inhibitor) was employed to confirm the initiation effect of Tau/CDs on the ferroptosis of RKO cells. Treatment with 10 μM Fer-1 notably attenuated the changes in cell viability, GSH depletion, MDA levels, iron accumulation, and ROS production in Tau/CDs-treated RKO cells (Supplementation Figure 9, $P<0.05$). These results underscored that the Tau/CDs-mediated ferroptosis drives their therapeutic efficacy in CRC progression.

HO-1 as a Critical Mediator of Tau/CDs-Induced Ferroptosis

The significant upregulation of HO-1, a well-established regulator of iron metabolism and ferroptosis, prompted further mechanistic investigation. Western blot and IF staining analyses confirmed elevated HO-1 expression both in vitro and in vivo following Tau/CDs treatment (Figure 8 & Supplementation Figures S7 & S8).

To establish the functional relevance of HO-1, RKO cells were co-treated with Tau/CDs and 10 μM zinc protoporphyrin-9 (ZnPP), a specific HO-1 inhibitor. ZnPP effectively reversed Tau/CDs-induced ferroptosis, as evidenced by the reductions in ROS production, MDA levels, iron accumulation, and GSH depletion, as well as the enhanced cell viability (Supplementation Figure 10, $P<0.05$).

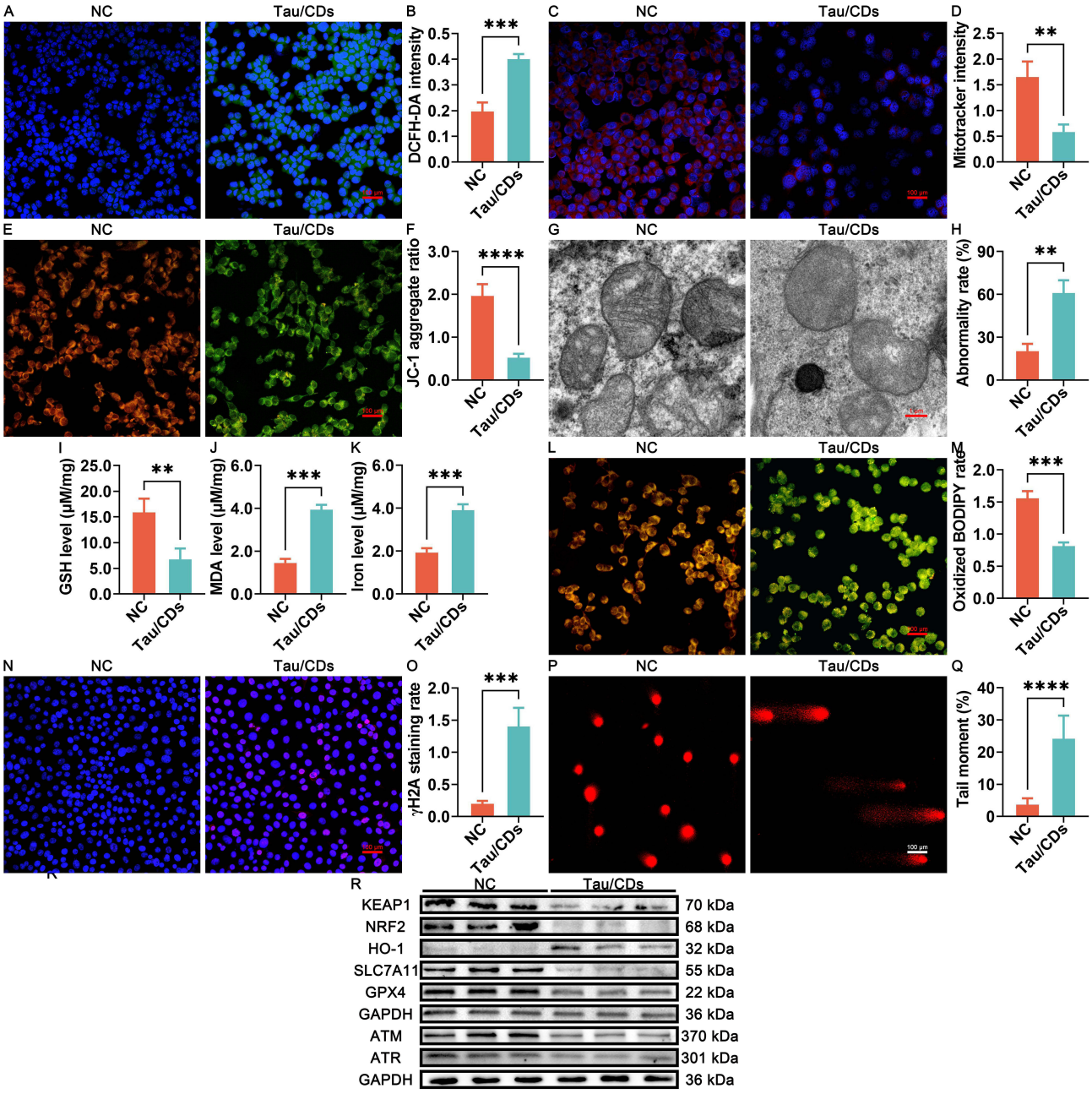

Figure 8 Tau/CDs induce ferroptosis and DNA damage in RKO cells. (**A**) DCFH-DA staining for intracellular ROS detection. (**B**) Quantitative analysis of DCFH-DA fluorescence intensity. (**C**) MitoTracker staining showing mitochondrial activity. (**D**) Quantitative analysis of MitoTracker fluorescence intensity. (**E**) JC-1 staining for mitochondrial membrane potential evaluation. (**F**) Quantification of JC-1 red/green fluorescence ratio. (**G**) TEM observation of mitochondrial ultrastructure. (**H**) Quantification of abnormal mitochondrial morphology. (**I**) Measurement of intracellular GSH levels. (**J**) Measurement of intracellular MDA levels. (**K**) Quantification of intracellular iron concentrations. (**L**) C11-BODIPY 581/591 staining for lipid peroxidation detection. (**M**) Quantification of C11-BODIPY fluorescence shift. (**N**) γH2A.X IF staining for DNA damage assessment. (**O**) Quantification of γH2A.X-positive cells. (**P**) DNA comet assay visualizing DNA strand breaks. (**Q**) Quantitative analysis of DNA tail moments. (**R**) Western blot detection of ferroptosis- and DNA damage-associated protein expression. ** represents P<0.01, with *** representing P<0.001 and **** representing P<0.0001.

Collectively, these findings strongly suggest that Tau/CDs-mediated ferroptosis in CRC cells may be facilitated by HO-1 upregulation, offering a promising therapeutic approach to limit CRC progression by inducing ferroptosis (Supplementation Figure 11).

https://doi.org/10.2147/IJN.S516926

Discussion

Since their serendipitous discovery during the electrophoretic purification of arc-synthesized carbon nanotubes in 2004, CDs have rapidly gained prominence as multifunctional nanomaterials, owing to their unique optical properties, tunable surface chemistry, and excellent biocompatibility.[35] Their small size, combined with high chemical stability, ease of functionalization, and low toxicity, has positioned CDs as promising candidates for applications ranging from bioimaging and biosensing to drug delivery and cancer therapy.[36,37] Among the expanding classes of hybrid nanomaterials, Tau/CDs are particularly compelling, combining the inherent biological activity of Tau, including antioxidant, anti-inflammatory, and anti-cancer properties, with the structural and functional versatility of CDs.[38,39] Despite their promising potential, reports on the synthesis and biomedical application of Tau/CDs remain scarce.

In this context, the present study employed a bottom-up microwave-assisted approach to synthesize Tau/CDs, using citric acid and urea as carbon and nitrogen sources and Tau as a reactive dopant, a strategy distinct from earlier methods such as the thermal decomposition route reported by Sharma et al in 2022.[19] This synthesis paradigm allows for precise control over particle morphology, composition, and surface functionality, offering a robust platform for biomedical exploration.[40,41] Notably, amino acid-functionalized CDs, including Tau-derived variants, have demonstrated enhanced photophysical and electronic properties, biocompatibility, and metal ion binding capacities, making them ideal for diverse applications in healthcare, catalysis, and environmental remediation.[42–45] However, systematic investigations into the biological performance and mechanistic underpinnings of Tau/CDs remain limited, highlighting the need for comprehensive studies.

Despite the promising applications of CDs in preclinical studies, challenges such as biocompatibility and cytotoxicity remain.[46] In line with previous studies, our findings demonstrate the favorable biocompatibility of Tau/CDs, as evidenced by the absence of significant changes in the pathological and physiological parameters of C57BL/6 and BALB/c nude mice treated with Tau/CDs. Additionally, we observed no cytotoxic effects of Tau/CDs on the proliferation of normal cells. Furthermore, Tau/CDs treatment significantly reduced the viability, proliferation, migration, invasion, adhesion, clonogenicity, and EMT of RKO cells. It also induced cell cycle arrest and apoptosis in these cells. In vivo, Tau/CDs treatment led to decreased proliferation, angiogenesis, and metastasis in xenograft tumor tissues, while enhancing apoptotic activity. These results strongly support the potent anti-cancer efficacy of Tau/CDs in inhibiting CRC progression by disrupting key malignant behaviors of CRC cells. Mechanistically, transcriptomic changes in Tau/CDs-treated RKO cells suggest that the observed anti-cancer effects are closely associated with the activation of ferroptosis. This was further confirmed by the elevated ROS production, mitochondrial dysfunction, increased lipid peroxidation, GSH depletion, and iron accumulation induced by Tau/CDs.

In 2003, Stockwell et al identified a novel form of non-apoptotic cell death process triggered by the small molecule erastin.[47] This discovery sparked a surge in research to elucidate the foundational regulation mechanism, culminating in the formal identification of "ferroptosis" in 2012.[48] As characterized by the iron-dependent lipid peroxidation and subsequent plasma membrane rupture, ferroptosis is profoundly modulated by various metabolic disruptions, including redox homeostasis, iron metabolism, mitochondrial function, and the metabolism of amino acids, sugars, and lipids, as well as numerous signaling pathways.[49] Ultimately, either induction or inhibition of ferroptosis drives the genetically, biochemically, immunologically, and morphologically distinct from other cell death modalities, including autophagy, apoptosis, pyroptosis, necroptosis, and unregulated necrosis.[50]

Recent advancements in understanding the molecular mechanisms of ferroptosis have highlighted its central roles in various pathologies, including aging, ischemic organ injuries, degenerative diseases, multiorgan dysfunction syndrome (MODS), and autoimmune conditions.[49,51] Most notably, ferroptosis is particularly implicated in a range of cancers, including breast, lung, gastrointestinal, and reproductive carcinomas, as well as lymphoma and melanoma.[52,53] Increasing evidence from datasets and clinical samples also underscores the involvement of ferroptosis-related molecules in CRC progression through multiple pathways. This has positioned ferroptosis as a promising target for CRC therapy, with potential as an effective tumor-suppressing mechanism within current treatment strategies.[54] Additionally, several therapeutic agents, including drugs such as bromelain, cetuximab, cisplatin, lapatinib, sulfasalazine, and paclitaxel, alongside natural products containing nutraceuticals and phytochemicals, as well as nanomaterials like graphene oxide,

are currently under clinical investigation for their ability to induce ferroptosis in CRC cells.[55–57] Notably, the integration of ferroptosis with conventional therapies, whether as standalone treatment, in combination with other methods, or alongside targeted therapy, has broadened the landscape of non-surgical options, including chemotherapy, radiotherapy, and immunotherapy.[58] This integration supports new avenues for early diagnosis, personalized treatment, and more precise prognostic strategies for CRC patients, as well as the key role of ferroptosis in CRC management.

Building on studies that demonstrate the promising effects of various nanomaterials in activating ferroptosis, such as zinc oxide coated virus-like silica nanoparticles,[59] $Na_2S_2O_8$-IR780 cascade nanoplatforms,[60] 6-gingerol-loaded magnetic mesoporous silicon nanoparticles functionalized with mulberry leaf-derived lipids and Pluronic F127,[61] rapamycin/resveratrol-loaded liposomes,[62] FexMoyS nanoparticles,[63] and Cu_2O@Au nanocomposites,[64] we identified a similar potential in Tau/CDs for inducing ferroptosis in RKO cells. In contrast, in 2024, Xiao et al observed that Tau inhibited ferroptosis in prostate cancer cells,[65] while Zhang et al reported similar ferroptosis inhibition by Tau in lung cancer cells.[66] Given the promising anti-cancer effect of Tau on CRC progression,[22,67,68] as well as the demonstrated ability of CDs to activate ferroptosis,[69–71] these divergent findings may stem from variations in cancer cell types or potential modifications in properties of Tau during CD preparation. This hypothesis requires further investigation to clarify the mechanisms involved. Moreover, the varying effects of CDs from different sources, whether promoting or inhibiting ferroptosis and potentially either accelerating or inhibiting cancer progression, highlight the multifaceted functionality of CDs depending on their resource, precursors, and synthetic strategies.[69,72,73] This complexity underscores the expanding interest in exploring CDs in clinical cancer treatments, where tailored approaches may leverage their diverse properties for optimized therapeutic outcomes for CRC patients.

Building on previous studies indicating that nanomaterials can activate ferroptosis by upregulating HO-1 expression,[74,75] our research is the first to demonstrate that Tau/CDs-mediated ferroptosis in CRC cells is positively associated with increased HO-1 expression. HO-1, also known as HMOX1, is an enzyme responsible for degrading heme into biliverdin, carbon monoxide (CO), and free ferrous iron. It possesses pro-oxidant, cytoprotective, and anti-inflammatory effects, and its role spans numerous pathological conditions, including diabetes, chronic obstructive pulmonary disease, myocardial infarction, thrombosis, sepsis, and SARS-CoV-2 infection. Prior research has established that upregulated HO-1 expression sensitizes cancer cells to ferroptosis,[76,77] and several studies suggest that elevated HO-1 expression significantly inhibited CRC progression by inducing ferroptosis in CRC cells,[78,79] aligning partly with our current findings. Additionally, research has also demonstrated that Tau treatments promote HO-1 expression in myocardial,[80] liver,[81] intestinal,[82] and neural tissues.[83] However, the specific regulatory effects of Tau/CDs on the upregulation of HO-1 in CRC cells remain to be fully explored.

While this study presents robust evidence supporting the anti-cancer potential of Tau/CDs via HO-1-mediated ferroptosis, several limitations warrant critical consideration. The current findings are predominantly derived from in vitro cancer cell models and murine xenograft systems, which, despite offering valuable mechanistic insights, fall short of recapitulating the intricate immunological, metabolic, and microenvironmental dynamics characteristic of human CRC. Key translational challenges, including nanoparticle pharmacokinetics, off-target biodistribution, and the heterogeneity inherent to patient-derived tumors, remain unresolved. Moreover, the precise molecular pathways by which Tau/CDs regulate HO-1 expression and trigger ferroptosis in human tissues demand further mechanistic dissection. In addition, the complex reactions between Tau and CDs on promoting the therapeutic efficacy of Tau need more detailed investigation. Despite these limitations, this work provides the first demonstration of Tau/CDs as a biocompatible, multifunctional nanoplatform capable of modulating ferroptosis, thereby underscoring both their mechanistic novelty and translational promise. Future investigations leveraging patient-derived organoids, advanced immunocompetent animal models, and clinical-grade pharmacological profiling will be essential to fully assess the therapeutic potential and safety of Tau/CDs, paving the way for their rational integration into next-generation CRC therapies.

Conclusion

In this study, we synthesized Tau/CDs using citric acid as the carbon source, urea as the nitrogen source, and Tau as the reactive dopant via microwave irradiation. Both in vitro and in vivo biosafety assessments demonstrated the excellent biocompatibility of Tau/CDs. Notably, Tau/CDs exhibited significant anti-cancer efficacy against CRC progression by

modulating key malignant behaviors of CRC cells, with the activation of HO-1-mediated ferroptosis identified as a potential mechanism. These findings highlight the promising potential of Tau/CDs as an anti-cancer agent for CRC treatment. However, further investigations are needed to fully elucidate the underlying mechanisms by which Tau/CDs regulate HO-1 expression and induce ferroptosis in CRC cells, thus advancing their therapeutic potential.

Abbreviations

Tau/CDs, Taurine-derived carbon dots; CRC, Colorectal cancer; EMT, Epithelial-mesenchymal transition; HO-1, Heme Oxygenase 1, CIN, chromosomal instability; MSI, Microsatellite instability; CIMP, CpG island methylation phenotype; CDs, Carbon quantum dots; TME, Tumor microenvironment; Tau, Taurine; TEM, Transmission electron microscopy; XPS, X-ray photoelectron spectroscopy; FTIR, Fourier transforms infrared; IACUC, Institution Animal Care and Use Committee; HUCMSCs, Human umbilical cord mesenchymal stem cells; FBS, Fetal bovine serum; P/S, Penicillin/streptomycin antibiotics; PBS, Phosphate-buffered saline; NC, Negative control; ALT, Alanine aminotransferase; AST, Aspartate aminotransferase; BUN, Blood urea nitrogen; CRE, Creatinine; H&E, Hematoxylin and eosin; PAS, Periodic acid Schiff; MTT, 3-(4,5-dimethylthiazol-2-yl-2,5-diphenyl tetrazolium bromide; DPBS, Dulbecco's phosphate-buffered saline; DMSO, Dimethyl sulfoxide solution; IR, Inhibiting rate; PFA, Paraformaldehyde; PI, Propidium iodide; FACS, Flow cytometry; TUNEL, Terminal deoxynucleotidyl transferase-mediated dUTP nick end-labeling; IF, Immunofluorescence; TdT, Terminal deoxynucleotidyl transferase; BSA, Bovine albumin solution; FPKM, Fragments per kilobase of exon per million fragments mapped; DEGs, Differentially expressed genes; FDR, False discovery rate; GO, Gene ontology; KEGG, Kyoto Genes and Genomes; DAVID, Database for Annotation, Visualization, and Integrated Discovery; GSEA, Gene Set Enrichment Analysis; DCFH-DA, Dichlorofluorescein diacetate; ΔΨm, Mitochondrial membrane potential; SDS-PAGE, Sodium Dodecyl Sulfate-Polyacrylamide Gel Electrophoresis; ECL, Enhanced chemiluminescence; SPSS, Statistical Package for the Social Sciences software; SD, Standard deviations; ns, Not significant; CS, Core-state; GSEA, Gene set enrichment analysis; Fer-1, Ferrostatin-1; ZnPP, Zinc protoporphyrin-9; MODS, Multiorgan dysfunction syndrome; CO, Carbon monoxide.

Acknowledgments

We gratefully acknowledge Miss Xiaomei Sun from the Affiliated Hospital of Inner Mongolia Medical University for her valuable expertise and support during this study.

Funding

This work was supported by the Natural Science Foundation of Inner Mongolia (Grant 2025MS08125 to Gang Liu), the National Natural Science Foundation of China (Grant 82360551 to Liya Su), the Outstanding Young Talents Cultivation Program of Grassland Elite in Inner Mongolia (Grant Q202286 to Gang Liu), the Zhiyuan Talents Cultivation Program of Mongolia Medical University (Grant ZY20242129 to Gang Liu), the Inner Mongolia Medical University Affiliated Hospital Talent Training Project-Sailing Series (Gang Liu), the United Foundation of Inner Mongolia Medical University (Grant YKD2024LH009 to Fangyuan Liu), the Higher Education Scientific Research Project of Inner Mongolia (Grant NJZY22674 to Fangyuan Liu), and the Natural Science Foundation of Shandong (Grant ZR2023QB261 to Mengqi Wang).

Disclosure

The authors declare no competing financial interests or personal relationships that could influence the findings of this study.

References

1. Eng C, Yoshino T, Ruíz-García E, et al. Colorectal cancer. *Lancet*. 2024;404(10449):294–310. doi:10.1016/S0140-6736(24)00360-X
2. Biller LH, Schrag D. Diagnosis and treatment of metastatic colorectal cancer. *JAMA*. 2021;325(7):669. doi:10.1001/jama.2021.0106
3. Sedlak JC, Yilmaz ÖH, Roper J. Metabolism and colorectal cancer. *Annu Rev Pathol -Mech*. 2023;18(1):467–492. doi:10.1146/annurev-pathmechdis-031521-041113
4. Abedizadeh R, Majidi F, Khorasani HR, Abedi H, Sabour D. Colorectal cancer: a comprehensive review of carcinogenesis, diagnosis, and novel strategies for classified treatments. *Cancer Metast Rev*. 2023;43(2):729–753. doi:10.1007/s10555-023-10158-3

5. Dekker E, Tanis PJ, Vleugels JLA, Kasi PM, Wallace MB. Colorectal cancer. *Lancet*. 2019;394(10207):1467–1480. doi:10.1016/S0140-6736(19)32319-0
6. Ding K, Mou P, Wang Z, et al. The next bastion to be conquered in immunotherapy: microsatellite stable colorectal cancer. *Front Immunol*. 2023;14:1298524. doi:10.3389/fimmu.2023.1298524
7. Underwood PW, Ruff SM, Pawlik TM. Update on targeted therapy and immunotherapy for metastatic colorectal cancer. *Cells*. 2024;13(3):245. doi:10.3390/cells13030245
8. Narayana S, Gowda BHJ, Hani U, et al. Inorganic nanoparticle-based treatment approaches for colorectal cancer: recent advancements and challenges. *J Nanobiotechnol*. 2024;22(1):427. doi:10.1186/s12951-024-02701-3
9. Strickler JH, Yoshino T, Graham RP, Siena S, Bekaii-Saab T. Diagnosis and treatment of ERBB2-positive metastatic colorectal cancer. *JAMA Oncol*. 2022;8(5):760. doi:10.1001/jamaoncol.2021.8196
10. Fan D, Cao Y, Cao M, Wang Y, Cao Y, Gong T. Nanomedicine in cancer therapy. *Signal Transduction Tar*. 2023;8(1):293.
11. Valcourt DM, Harris J, Riley RS, Dang M, Wang J, Day ES. Advances in targeted nanotherapeutics: from bioconjugation to biomimicry. *Nano Res*. 2018;11(10):4999–5016. doi:10.1007/s12274-018-2083-z
12. Lou W, Xie L, Xu L, et al. Present and future of metal nanoparticles in tumor ablation therapy. *Nanoscale*. 2023;15(44):17698–17726. doi:10.1039/D3NR04362B
13. Jain A, Bhattacharya S. Recent advances in nanomedicine preparative methods and their therapeutic potential for colorectal cancer: a critical review. *Front Oncol*. 2023;13:1211603. doi:10.3389/fonc.2023.1211603
14. Kong J, Wei Y, Zhou F, et al. Carbon quantum dots: properties, preparation, and applications. *Molecules*. 2024;29(9):2002. doi:10.3390/molecules29092002
15. Kolanowska A, Dzido G, Krzywiecki M, et al. Carbon quantum dots from amino acids revisited: survey of renewable precursors toward high quantum-yield blue and green fluorescence. *ACS Omega*. 2022;7(45):41165–41176. doi:10.1021/acsomega.2c04751
16. Đorđević L, Arcudi F, Prato M. Preparation, functionalization and characterization of engineered carbon nanodots. *Nat Protoc*. 2019;14(10):2931–2953. doi:10.1038/s41596-019-0207-x
17. Singh P, Gollapalli K, Mangiola S, et al. Taurine deficiency as a driver of aging. *Science*. 2023;380(6649):eabn9257. doi:10.1126/science.abn9257
18. Wang L, Xie Z, Wu M, et al. The role of taurine through endoplasmic reticulum in physiology and pathology. *Biochem Pharmacol*. 2024;226:116386. doi:10.1016/j.bcp.2024.116386
19. Sharma A, Kundu M, Ghosh N, et al. Synthesis of carbon dots from taurine as bioimaging agent and nanohybrid with ceria for antioxidant and antibacterial applications. *Photodiagnosis Photodyn Ther*. 2022;39:102861. doi:10.1016/j.pdpdt.2022.102861
20. Hu A, Chen G, Huang A, et al. o-phenylenediamine derived fluorescent carbon quantum dots for detection of Hg(II) in environmental water. *J Fluoresc*. 2023;34(2):905–913. doi:10.1007/s10895-023-03331-y
21. Tu S, Zhang XL, Wan HF, et al. Effect of taurine on cell proliferation and apoptosis human lung cancer A549 cells. *Oncol Lett*. 2018;15(4):5473–5480. doi:10.3892/ol.2018.8036
22. Chen CX, Wan HF, Li SY, Wan FS. The inhibition of the invasion and metastasis of colorectal cancer cells by taurine through regulation of the PTEN/AKT/GSK-3β pathway. *Asian J Surg*. 2022;45(3):970–973. doi:10.1016/j.asjsur.2021.12.049
23. Wang M, Lan S, Zhang W, et al. Anti-cancer potency of copper-doped carbon quantum dots against breast cancer progression. *Int J Nanomed*. 2024;19:1985–2004. doi:10.2147/IJN.S449887
24. Liu J-Y, Yen C-H, Lin Y-F, Feng Y-H, Fang Y-P. Improving the thrombocytopenia adverse reaction of belinostat using human serum albumin nanoparticles. *Int J Nanomed*. 2024;19:10785–10800. doi:10.2147/IJN.S475823
25. Zhang W, Sun J, Lan S, et al. Regulation of Fuzheng Huayu capsule on inhibiting the fibrosis-associated hepatocellular carcinogenesis. *J Asian Nat Prod Res*. 2024;26(10):1219–1238. doi:10.1080/10286020.2024.2355132
26. Jin Q, Dai Y, Wang Y, Zhang S, Liu G. High kinesin family member 11 expression predicts poor prognosis in patients with clear cell renal cell carcinoma. *J Clin Pathol*. 2019;72(5):354–362. doi:10.1136/jclinpath-2018-205390
27. Zhang X, Tu S, Wang Y, Xu B, Wan F. Mechanism of taurine-induced apoptosis in human colon cancer cells. *Acta Bioch Bioph Sin*. 2014;46(4):261–272. doi:10.1093/abbs/gmu004
28. Park YJ, Choi SH, Lee JY, Suh JS, Park YS, Chung CP. Dual-function synthetic peptide derived from BMP4 for highly efficient tumor targeting and antiangiogenesis. *Int J Nanomed*. 2016;11:4643–4656. doi:10.2147/IJN.S115044
29. Jin Q, Liu G, Li S, et al. Decellularized breast matrix as bioactive microenvironment for in vitro three-dimensional cancer culture. *J Cell Physiol*. 2019;234(4):3425–3435. doi:10.1002/jcp.26782
30. Li S, Liu M, Ma H, et al. Ameliorative effect of recombinant human lactoferrin on the premature ovarian failure in rats after cyclophosphamide treatments. *J Ovarian Res*. 2021;14(1):17. doi:10.1186/s13048-020-00763-z
31. Wang M, Ren J, Liu Z, et al. Beneficial effect of selenium doped carbon quantum dots supplementation on the in vitro development competence of ovine oocytes. *Int J Nanomed*. 2022;17:2907–2924. doi:10.2147/IJN.S360000
32. Wu Y, Sun C. Salidroside prevents cadmium chloride-induced DNA damage in human fetal lung fibroblasts. *J Trace Elem Med Bio*. 2024;86:127521. doi:10.1016/j.jtemb.2024.127521
33. Zhang W, Sun J, Liu F, et al. Alleviative effect of lactoferrin interventions against the hepatotoxicity induced by titanium dioxide nanoparticles. *Biol Trace Elem Res*. 2023;202(2):624–642. doi:10.1007/s12011-023-03702-3
34. Wu H, Liu Q, Shan X, Gao W, Chen Q. ATM orchestrates ferritinophagy and ferroptosis by phosphorylating NCOA4. *Autophagy*. 2023;19(7):2062–2077. doi:10.1080/15548627.2023.2170960
35. Xu X, Ray R, Gu Y, et al. Electrophoretic analysis and purification of fluorescent single-walled carbon nanotube fragments. *J Am Chem Soc*. 2004;126(40):12736–12737. doi:10.1021/ja040082h
36. Shen C-L, Liu H-R, Lou Q, et al. Recent progress of carbon dots in targeted bioimaging and cancer therapy. *Theranostics*. 2022;12(6):2860–2893. doi:10.7150/thno.70721
37. Bayda S, Amadio E, Cailotto S, Frión-Herrera Y, Perosa A, Rizzolio F. Carbon dots for cancer nanomedicine: a bright future. *Nanoscale Adv*. 2021;3(18):5183–5221. doi:10.1039/D1NA00036E
38. Qiu S, Li X, Zhang J, et al. Neutrophil membrane-coated taurine nanoparticles protect against hepatic ischemia-reperfusion injury. *Eur J Pharmacol*. 2023;949:175712. doi:10.1016/j.ejphar.2023.175712

39. Baysal G, Demirci C, Özpinar H. Properties and synthesis of biosilver nanofilms for antimicrobial food packaging. *Polymers*. 2023;15(3):689. doi:10.3390/polym15030689
40. Qureshi ZA, Dabash H, Ponnamma D, Abbas MKG. Carbon dots as versatile nanomaterials in sensing and imaging: efficiency and beyond. *Heliyon*. 2024;10(11):e31634. doi:10.1016/j.heliyon.2024.e31634
41. Jing HH, Shati AA, Alfaifi MY, Elbehairi SEI, Sasidharan S. The future of plant based green carbon dots as cancer Nanomedicine: from current progress to future perspectives and beyond. *J Adv Res*. 2025;67:133–159. doi:10.1016/j.jare.2024.01.034
42. Ravi PV, Subramaniyam V, Pattabiraman A, Pichumani M. Do amino acid functionalization stratagems on carbonaceous quantum dots imply multiple applications? A comprehensive review. *RSC Adv*. 2021;11(55):35028–35045. doi:10.1039/D1RA05571B
43. Pandit S, Behera P, Sahoo J, De M. In situ synthesis of amino acid functionalized carbon dots with tunable properties and their biological applications. *Acs Appl Bio Mater*. 2019;2(8):3393–3403. doi:10.1021/acsabm.9b00374
44. Kumar VB, Mirsky SK, Shaked NT, Gazit E. High quantum yield amino acid carbon quantum dots with unparalleled refractive index. *ACS Nano*. 2024;18(3):2421–2433. doi:10.1021/acsnano.3c10792
45. Zhang Y, Zhang S, Tan B, Guo L, Li H. Solvothermal synthesis of functionalized carbon dots from amino acid as an eco-friendly corrosion inhibitor for copper in sulfuric acid solution. *J Colloid Interf Sci*. 2021;604:1–14. doi:10.1016/j.jcis.2021.07.034
46. Kharlamova M, Kramberger C. Cytotoxicity of carbon nanotubes, graphene, fullerenes, and dots. *Nanomaterials*. 2023;13(9):1458. doi:10.3390/nano13091458
47. Dolma S, Lessnick SL, Hahn WC, Stockwell BR. Identification of genotype-selective antitumor agents using synthetic lethal chemical screening in engineered human tumor cells. *Cancer Cell*. 2003;3(3):285–296. doi:10.1016/S1535-6108(03)00050-3
48. Dixon SJ, Lemberg KM, Lamprecht MR, et al. Ferroptosis: an iron-dependent form of nonapoptotic cell death. *Cell*. 2012;149(5):1060–1072. doi:10.1016/j.cell.2012.03.042
49. Jiang X, Stockwell BR, Conrad M. Ferroptosis: mechanisms, biology and role in disease. *Nat Rev Mol Cell Biol*. 2021;22(4):266–282. doi:10.1038/s41580-020-00324-8
50. Stockwell BR, Friedmann Angeli JP, Bayir H, et al. Ferroptosis: a regulated cell death nexus linking metabolism, redox biology, and disease. *Cell*. 2017;171(2):273–285. doi:10.1016/j.cell.2017.09.021
51. Liang D, Feng Y, Zandkarimi F, et al. Ferroptosis surveillance independent of GPX4 and differentially regulated by sex hormones. *Cell*. 2023;186(13):2748–2764.e22. doi:10.1016/j.cell.2023.05.003
52. Yan H, Talty R, Aladelokun O, Bosenberg M, Johnson CH. Ferroptosis in colorectal cancer: a future target? *Br J Cancer*. 2023;128(8):1439–1451. doi:10.1038/s41416-023-02149-6
53. Kao AT, Cabanlong CV, Padilla K, Xue X. Unveiling ferroptosis as a promising therapeutic avenue for colorectal cancer and colitis treatment. *Acta Pharmaceutica Sinica B*. 2024;14(9):3785–3801. doi:10.1016/j.apsb.2024.05.025
54. Fan S, Zhou L, Zhang W, Wang D, Tang D. Ferroptosis: the balance between death and survival in colorectal cancer. *Int J Biol Sci*. 2024;20(10):3773–3783. doi:10.7150/ijbs.96828
55. Bi Y, Li Y, Li W, et al. Research progress on ferroptosis in colorectal cancer. *Front Immunol*. 2024;15:1462505. doi:10.3389/fimmu.2024.1462505
56. Zhang Y, Xie J. Targeting ferroptosis regulators by natural products in colorectal cancer. *Front Pharmacol*. 2024;15:1374722. doi:10.3389/fphar.2024.1374722
57. Zhou X, Zhang Q, Zhu H, Zhao J, Cai Y. The application of graphene oxide and ferroptosis in the diagnosis and treatment of colorectal cancer: a narrative review. *J Gastrointest Oncol*. 2024;15(3):1297–1308. doi:10.21037/jgo-23-1016
58. Yang J, Pan C, Zhang J, et al. Exploring the potential of biocompatible osmoprotectants as highly efficient cryoprotectants. *Acs Appl Mater Inter*. 2017;9(49):42516–42524. doi:10.1021/acsami.7b12189
59. Pan X, Qi Y, Du Z, et al. Zinc oxide nanosphere for hydrogen sulfide scavenging and ferroptosis of colorectal cancer. *J Nanobiotechnol*. 2021;19(1):392. doi:10.1186/s12951-021-01069-y
60. Shi J, Tian H, Peng L, et al. A nanoplatform reshaping intracellular osmolarity and redox homeostasis against colorectal cancer. *J Control Release*. 2022;352:766–775. doi:10.1016/j.jconrel.2022.11.003
61. Li B, Zu M, Jiang A, et al. Magnetic natural lipid nanoparticles for oral treatment of colorectal cancer through potentiated antitumor immunity and microbiota metabolite regulation. *Biomaterials*. 2024;307:122530. doi:10.1016/j.biomaterials.2024.122530
62. Jia M, Tan X, Yuan Z, Zhu W, Yan P. Nanoliposomes encapsulated rapamycin/resveratrol to induce apoptosis and ferroptosis for enhanced colorectal cancer therapy. *J Pharm Sci*. 2024;113(8):2565–2574. doi:10.1016/j.xphs.2024.05.015
63. Yu Z, Wang C, Ye Y, Wang S, Jiang K. Therapeutic potentials of FexMoyS-PEG nanoparticles in colorectal cancer: a multimodal approach via ROS-ferroptosis-glycolysis regulation. *J Nanobiotechnol*. 2024;22(1):253. doi:10.1186/s12951-024-02515-3
64. Lin X, Chen H, Deng T, et al. Improved immune response for colorectal cancer therapy triggered by multifunctional nanocomposites with self-amplifying antitumor ferroptosis. *Acs Appl Mater Inter*. 2024;16(11):13481–13495. doi:10.1021/acsami.3c16813
65. Xiao H, Du X, Tao Z, et al. Taurine inhibits ferroptosis mediated by the crosstalk between tumor cells and tumor-associated macrophages in prostate cancer. *Adv Sci*. 2023;11(3):e2303894. doi:10.1002/advs.202303894
66. Zhang X, Xu Y, Ma L, et al. Essential roles of exosome and circRNA_101093 on ferroptosis desensitization in lung adenocarcinoma. *Cancer Commun*. 2022;42(4):287–313. doi:10.1002/cac2.12275
67. Liu Z, Xia Y, Zhang X, et al. Roles of the MST1-JNK signaling pathway in apoptosis of colorectal cancer cells induced by Taurine. *Libyan J Med*. 2018;13(1):1500346. doi:10.1080/19932820.2018.1500346
68. Wang G, Ma N, He F, et al. Taurine attenuates carcinogenicity in ulcerative colitis-colorectal cancer mouse model. *Oxid Med Cell Longev*. 2020;2020:7935917. doi:10.1155/2020/7935917
69. Bao Y, Li G, Li S, et al. Multifunctional tumor-targeting carbon dots for tumor microenvironment activated ferroptosis and immunotherapy in cancer treatment. *ACS Appl Mater Interfaces*. 2023. doi:10.1021/acsami.3c13867
70. Zhou M, Yang Z, Yin T, et al. Functionalized Fe-doped carbon dots exhibiting dual glutathione consumption to amplify ferroptosis for enhanced cancer therapy. *Acs Appl Mater Inter*. 2023;15(46):53228–53241. doi:10.1021/acsami.3c12356
71. Li H, Dou Y, Yang H, et al. Ce6-modified Fe ions-doped carbon dots as multifunctional nanoplatform for ferroptosis and photodynamic synergistic therapy of melanoma. *J Nanobiotechnol*. 2024;22(1):100. doi:10.1186/s12951-024-02346-2

72. Li J, Fu C, Feng B, et al. Polyacrylic acid-coated selenium-doped carbon dots inhibit ferroptosis to alleviate chemotherapy-associated acute kidney injury. *Adv Sci*. 2024;11(28):e2400527. doi:10.1002/advs.202400527
73. Wang Z, Han J, Guo Z, et al. Ginseng-based carbon dots inhibit the growth of squamous cancer cells by increasing ferroptosis. *Front Oncol*. 2023;13:1097692. doi:10.3389/fonc.2023.1097692
74. Wang L, Wang T, Zhuo Y, et al. Cascade Co8FeS8@Co1-xS nano-enzymes trigger efficiently apoptosis-ferroptosis combination tumor therapy. *J Colloid Interf Sci*. 2024;662:962–975. doi:10.1016/j.jcis.2024.01.153
75. Fu S, Li Y, Shen L, et al. Cu(2)WS(4)-PEG nanozyme as multifunctional sensitizers for enhancing immuno-radiotherapy by inducing ferroptosis. *Small*. 2024;20(26):e2309537. doi:10.1002/smll.202309537
76. Zheng C, Zhang B, Li Y, et al. Donafenib and GSK-J4 synergistically induce ferroptosis in liver cancer by upregulating HMOX1 expression. *Adv Sci*. 2023;10(22):e2206798. doi:10.1002/advs.202206798
77. Wang Z, Li W, Wang X, et al. Isoliquiritigenin induces HMOX1 and GPX4-mediated ferroptosis in gallbladder cancer cells. *Chin Med J*. 2023;136 (18):2210–2220. doi:10.1097/CM9.0000000000002675
78. Rah B, Shafarin J, Karim A, Bajbouj K, Hamad M, Muhammad JS. Iron overloading potentiates the antitumor activity of 5-fluorouracil by promoting apoptosis and ferroptosis in colorectal cancer cells. *Cell Biochem Biophys*. 2024;82(4):3763–3780. doi:10.1007/s12013-024-01463-x
79. Chen M, Ma S, Ji W, et al. Shenqi Sanjie Granules induce Hmox1-mediated ferroptosis to inhibit colorectal cancer. *Heliyon*. 2024;10(18):e38021. doi:10.1016/j.heliyon.2024.e38021
80. Wang GG, Li W, Lu XH, Zhao X, Xu L. Taurine attenuates oxidative stress and alleviates cardiac failure in type I diabetic rats. *Croat Med J*. 2013;54(2):171–179. doi:10.3325/cmj.2013.54.171
81. Liu Y, Li F, Zhang L, Wu J, Wang Y, Yu H. Taurine alleviates lipopolysaccharide-induced liver injury by anti-inflammation and antioxidants in rats. *Mol Med Rep*. 2017;16(5):6512–6517. doi:10.3892/mmr.2017.7414
82. Hassanein EHM, Althagafy HS, Atwa AM, Kozman MR, Kotb El-Sayed MI, Soubh AA. Taurine attenuated methotrexate-induced intestinal injury by regulating NF-κB/iNOS and Keap1/Nrf2/HO-1 signals. *Life Sci*. 2022;311(Pt A):121180. doi:10.1016/j.lfs.2022.121180
83. Lee DS, Cheong SH. Taurine have neuroprotective activity against oxidative damage-induced HT22 cell death through heme oxygenase-1 pathway. *Adv Exp Med Biol*. 2017;975 Pt 1:159–171.